

Gate Freezing Method for Gradient-Free Variational Quantum Algorithms in Circuit Optimization

Joona V. Pankkonen,^{*} Matti Raasakka, Andrea Marchesin, and Ilkka Tittonen

*Micro and Quantum Systems group,
Department of Electronics and Nanoengineering,
Aalto University, Finland*

Lauri Ylinen

*Department of Mathematics and Statistics,
University of Jyväskylä, Finland*

(Dated: July 11, 2025)

Parameterized quantum circuits (PQCs) are pivotal components of variational quantum algorithms (VQAs), which represent a promising pathway to quantum advantage in noisy intermediate-scale quantum (NISQ) devices. PQCs enable flexible encoding of quantum information through tunable quantum gates and have been successfully applied across domains such as quantum chemistry, combinatorial optimization, and quantum machine learning. Despite their potential, PQC performance on NISQ hardware is hindered by noise, decoherence, and the presence of barren plateaus, which can impede gradient-based optimization. To address these limitations, we propose novel methods for improving gradient-free optimizers **Rotosolve**, **Fraxis**, and **FQS**, incorporating information from previous parameter iterations. Our approach conserves computational resources by reallocating optimization efforts toward poorly optimized gates, leading to improved convergence. The experimental results demonstrate that our techniques consistently improve the performance of various optimizers, contributing to more robust and efficient PQC optimization.

I. INTRODUCTION

Parameterized quantum circuits (PQCs) are an essential component of variational quantum algorithms (VQAs), which have emerged as leading candidates to achieve quantum advantage on near-term devices [1, 2]. PQCs provide a flexible and expressive framework for encoding quantum information and solving computational problems in domains such as quantum chemistry [3–7], combinatorial optimization [8–10], and quantum machine learning [11–14]. A PQC comprises a sequence of quantum gates with tunable parameters. By optimizing these parameters using a classical feedback loop, the circuit can approximate solutions to complex problems that are classically intractable [15, 16]. In particular, PQCs have been successfully applied to simulate molecular ground states [17, 18], and solve Max-Cut and other NP-hard problems [19–21]. Their adaptability and compatibility with noisy intermediate-scale quantum (NISQ) hardware make them a central building block in current hybrid quantum-classical computing paradigms [1, 22].

Despite the potential of PQCs, their deployment on NISQ devices introduces significant challenges. However, they are still able to provide quantum advantages to some extent to the aforementioned problems [23, 24]. Current quantum hardware is limited by decoherence, gate fidelity, and readout errors, affecting the precision and convergence of the optimization process [25, 26].

The presence of barren plateaus can make gradient-based methods inefficient or infeasible in PQC optimization

[27, 28]. As such, the development of parameter initialization techniques has been proposed, Gaussian initialization [29], Gaussian mixture model [30], reduced domain [31] as well as the parameter reuse strategy proposed in [32] for the Quantum Approximate Optimization Algorithm (QAOA) [33]. Sequential and subset-based optimization techniques improve the training efficiency of PQCs by updating only selected parameters or layers in each iteration, rather than the entire parameter set [34, 35].

In this work, we develop methods for various sequential single-qubit gate optimizers by incorporating parameter values from previous iterations into the circuit optimization process. The methods are motivated by the observation that typically after only a few iterations in the optimization process, a large subset of the parameters (e.g. angles or unit vectors) in the PQC start to change only very small amounts from iteration to iteration (See Fig. 1). Thus, by concentrating the optimization steps only to the parameters with significant change between iterations we are able to conserve available computational resources during the optimization process. This results in better convergence across several optimization runs for all optimizers.

This work is structured as follows. First, in Sec. II we go through the general optimization of PQCs as well as the gradient-free optimizers **Rotosolve** [36], **Free-Axis Selection (Fraxis)** [37] and **Free-Quaternion Selection (FQS)** [38]. Then, in Sec. III we present the proposed gate-freezing method that uses gate parameter values and a generalized version that uses matrix norms. In addition, we present the incremental gate freezing method for optimizing PQC. Next, we demonstrate how to incorpo-

^{*} Corresponding author: joona.pankkonen@aalto.fi

rate gate freezing methods into gradient-free optimizers. We provide results for the one-dimensional Heisenberg model as well as the Fermi-Hubbard lattice model. We also examined the scalability of the gate freezing method with the `Rotosolve` optimizer with various system sizes for the one-dimensional Heisenberg model in Sec. IV. Finally, in Sec. V we conclude our work and discuss further research ideas.

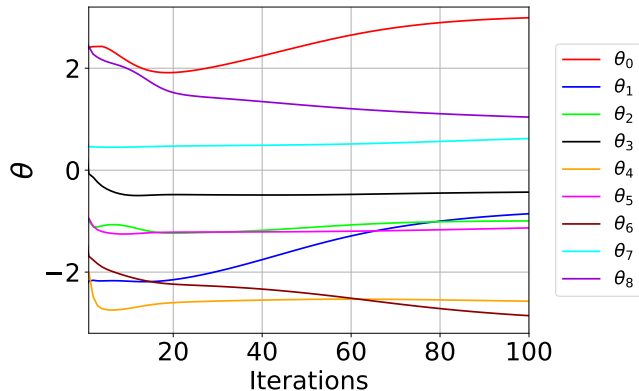


FIG. 1: A typical parameter evolution over time for randomly chosen angles $\theta_k \in [-\pi, \pi)$ in the PCQ using `Rotosolve` optimizer. One-dimensional Heisenberg model with 5 qubits and 3 layers were used with ansatz in Fig. 3.

II. OPTIMIZATION OF PARAMETERIZED QUANTUM CIRCUITS

A. Parameterized Quantum Circuits

We start by considering a PQC, which corresponds to a unitary $U(\theta)$ consisting of parameters θ [1]. The PQC unitary $U(\theta)$ usually consists of a layer of parameterized single-qubit gates in each qubit, followed by an entangling layer of two-qubit gates, usually Controlled-Z or CNOT gates. This structure is repeated L times, and the entire PQC unitary $U(\theta)$ can be written as $U(\theta) = U_L(\theta_L) \cdots U_1(\theta_1)$.

Now, if we follow the setting from [39] and denote the number of qubits by n , the single layer unitary $U_l(\theta_l)$ of the PQC can be expressed as follows:

$$U_l(\theta_l) = W_l \left(\bigotimes_{k=0}^{n-1} e^{-i\theta_{n(l-1)+k} H_{n(l-1)+k}/2} \right), \quad (1)$$

where W_l is the entangling layer and the index k runs over the individual qubits. The variable $\theta_{n(l-1)+k}$ denotes the k -th element in the parameter θ_l and $H_{n(l-1)+k}$ is a Hermitian operator that generates the unitary that acts on the k -th qubit in the l -th layer. An illustration of a PQC structure is shown in Fig. 2.

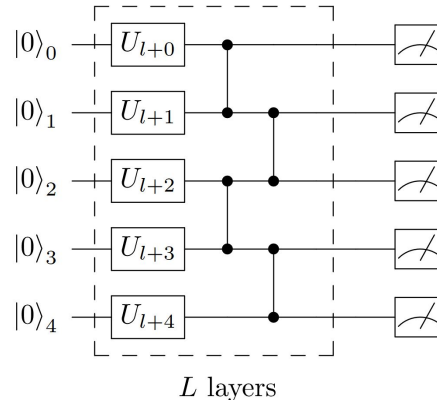


FIG. 2: Ansatz circuit design for PQC optimization for `Fraxis` and `FQS` optimizers.

To optimize the PQC, we need to define a cost function $C(\theta)$, which depends on the values of the parameter vector θ [40]. The cost function gives us a quantitative measure of how well the PQC is optimized. The cost function $C(\theta)$ is written as the expectation value of some Hermitian observable \hat{M} as follows

$$\langle \hat{M} \rangle = \text{Tr} \left(\hat{M} U(\theta) \rho_0 U(\theta)^\dagger \right), \quad (2)$$

where ρ_0 is the initial state of the PQC that is set to $\rho_0 = |\mathbf{0}\rangle\langle\mathbf{0}|$. Here, we denote the n -qubit state as $|\mathbf{0}\rangle \equiv |0\rangle^{\otimes n}$.

For the next subsections, we follow a similar setting as in Ref. [39] for the known VQAs `Rotosolve`, `Fraxis`, and `FQS`.

B. Rotosolve Optimizer

In this section, we generally describe how the gradient-free optimizer, `Rotosolve` [36] works. First, we consider that one ansatz circuit layer $U_l(\theta_l)$ consists of $2n$ different parameterized single-qubit gates. In this setting, two single-qubit gates act on each qubit in sequence, R_X and R_Y gates, respectively, followed by the entanglement layer W_l . Then the layer unitary $U_l(\theta_l)$ becomes

$$U_l(\theta_l) = W_l \left(\bigotimes_{k=0}^{n-1} e^{-i\theta_{n(2l-1)+k} H_{n(2l-1)+k}/2} \right) \left(\bigotimes_{k'=0}^{n-1} e^{-i\theta_{2n(l-1)+k'} H_{2n(l-1)+k'}/2} \right). \quad (3)$$

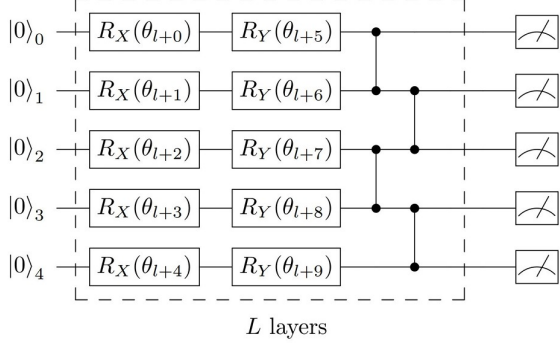


FIG. 3: Ansatz circuit design for Rotosolve algorithm with 5 qubits.

Here, the Hermitian operators $H_{2n(l-1)+k'}$ and $H_{n(2l-1)+k}$ denote the Pauli X and Y operators according to Fig. 3, respectively.

The ansatz circuit has a total of L layers. Then, the entire vector θ consists of the $2Ln$ parameters $\theta =$

$$\begin{aligned} \langle \hat{M} \rangle = & \text{Tr} \left(\hat{M} W_L R'_{2Ln-1}(\theta_{2Ln-1}) \cdots W_l R'_{2ln-1}(\theta_{2ln-1}) \cdots R'_{d+1}(\theta_{d+1}) R'_d(\theta_d) R'_{d-1}(\theta_{d-1}) \cdots R'_1(\theta_1) R'_0(\theta_0) \right. \\ & \left. \times \rho_0 R'_0(\theta_0)^\dagger R'_1(\theta_1)^\dagger \cdots R'_{d-1}(\theta_{d-1})^\dagger R'_d(\theta_d)^\dagger R'_{d+1}(\theta_{d+1})^\dagger \cdots R'_{2ln-1}(\theta_{2ln-1})^\dagger W_l^\dagger \cdots R'_{2Ln-1}(\theta_{2Ln-1})^\dagger W_L^\dagger \right). \end{aligned} \quad (6)$$

Now, we define the quantum circuits that come before and after the d -th parameterized gate R'_d as V_1 and V_2 , respectively. This allows us to write Eq. (6) in more compact form

$$\langle \hat{M} \rangle = \text{Tr} \left(\hat{M} V_1 R'_d(\theta_d) V_2 \rho_0 V_2^\dagger R'_d(\theta_d)^\dagger V_1^\dagger \right). \quad (7)$$

By further applying the cyclic property of the trace operation, we can absorb the quantum circuits V_1 and V_2 into the new variables M and ρ as follows

$$\rho \equiv V_2 \rho_0 V_2^\dagger, \quad (8)$$

$$M \equiv V_1^\dagger \hat{M} V_1. \quad (9)$$

Finally, we obtain the relevant form of the cost function similar to Refs. [36, 37, 39]

$$\langle M \rangle = \text{Tr} \left(M R'_d(\theta_d) \rho R'_d(\theta_d)^\dagger \right). \quad (10)$$

$(\theta_0, \dots, \theta_{2Ln-1})$. An illustration of this circuit is shown in Fig. 3.

The d -th single qubit rotation gate R_d ($d = 0, \dots, 2Ln - 1$) with the parameter $\theta_d \in (-\pi, \pi]$ is defined as [41]

$$R_d(\theta_d) = \cos\left(\frac{\theta_d}{2}\right) I - i \sin\left(\frac{\theta_d}{2}\right) H_d. \quad (4)$$

Here, H_d is the Hermitian unitary generator that satisfies the condition $H_d^2 = I$ and I is the 2×2 identity matrix. To operate the gate R_d in the circuit on the k -th qubit, it needs to be represented as a $2^n \times 2^n$ unitary matrix. We achieve this by applying a tensor product with 2×2 identity matrices as follows:

$$\begin{aligned} R'_d(\theta_d) = & I \otimes \cdots \otimes I \otimes \left[\cos\left(\frac{\theta_d}{2}\right) I - i \sin\left(\frac{\theta_d}{2}\right) H_d \right] \\ & \otimes I \otimes \cdots \otimes I, \end{aligned} \quad (5)$$

where before the gate R_d precedes a tensor product of identity matrices of length $k - 1$ and is followed by the length of $n - k$ tensor products of the identity matrices.

By applying Eq. (5) to Eq. (3), we obtain the following form for the cost function [39]

By using Eq. (4), the cost function becomes [36]

$$\begin{aligned} \langle M \rangle_{\theta_d} = & \cos^2\left(\frac{\theta_d}{2}\right) \text{Tr}(M \rho) \\ & + i \cos\left(\frac{\theta_d}{2}\right) \sin\left(\frac{\theta_d}{2}\right) \text{Tr}(M [\rho, H'_d]) \\ & + \sin^2\left(\frac{\theta_d}{2}\right) \text{Tr}(M H'_d \rho H'_d). \end{aligned} \quad (11)$$

Here, H'_d is a $2^n \times 2^n$ matrix that consists of a tensor product of the Hermitian generator H_d and 2×2 identity matrices. This follows straight from Eq. (5). By evaluating the cost function at angles $\theta_d = -\pi/2, 0, \pi/2$ and π , one can solve the values for the traces in Eq. (11). After that, the cost function $\langle M \rangle_{\theta_d}$ can be written as $\langle M \rangle_{\theta_d} = A \sin(\theta_d + B) + C$, where the coefficients A, B and C are combinations of measurements at different angles θ_d [36]. The minimum of the cost function is located at $\theta_d^* = -\frac{\pi}{2} - B + 2\pi m$, where $m \in \mathbb{Z}$ and the coefficient B defined as

$$\begin{aligned} B = & \arctan 2(2\langle M \rangle_\phi - \langle M \rangle_{\phi+\frac{\pi}{2}} - \langle M \rangle_{\phi-\frac{\pi}{2}}), \\ & \langle M \rangle_{\phi+\frac{\pi}{2}} - \langle M \rangle_{\phi-\frac{\pi}{2}} - \phi. \end{aligned} \quad (12)$$

Here, $\phi \in \mathbb{R}$ and it can be chosen arbitrarily. We chose to set it to zero in this work. The minimum value for the angle θ_d can finally be written as follows (see Ref. [36])

$$\begin{aligned}\theta_d^* &= \arg \min_{\theta_d} \langle M \rangle_{\theta_d} \\ &= -\frac{\pi}{2} - \arctan 2(2\langle M \rangle_{\phi} - \langle M \rangle_{\phi+\frac{\pi}{2}} - \langle M \rangle_{\phi-\frac{\pi}{2}}), \\ &\quad \langle M \rangle_{\phi+\frac{\pi}{2}} - \langle M \rangle_{\phi-\frac{\pi}{2}} + 2\pi n\end{aligned}\quad (13)$$

C. Free-Axis Selection Optimizer

In this and the following sections, we will go through two matrix diagonalization optimizers for the single-qubit gate optimization, **Fraxis** [37] and **FQS** [38]. The **Fraxis** optimizer works like a **Rotosolve** optimizer: it is a sequential single-qubit gate optimizer, which optimizes the PQC one gate at a time and uses circuit evaluations to determine the optimal rotation axis of the gate with a fixed rotation angle $\theta_d = \pi$.

Instead of a fixed axis of rotation (i.e. R_X , R_Y or R_Z), we represent the d -th rotation gate R_d ($d = 0, \dots, Ln-1$) with a rotation angle θ_d and a unit vector $\hat{\mathbf{n}}_d$ as follows [37]

$$\begin{aligned}R_d(\theta_d) &= e^{-i\frac{\theta_d}{2}\hat{\mathbf{n}}_d \cdot \boldsymbol{\sigma}} = \cos\left(\frac{\theta_d}{2}\right)I - i\sin\left(\frac{\theta_d}{2}\right)\hat{\mathbf{n}} \cdot \boldsymbol{\sigma} \\ &\equiv R_{\hat{\mathbf{n}}}(\theta_d),\end{aligned}\quad (14)$$

where $\boldsymbol{\sigma} = (X, Y, Z)$ are the Pauli matrices and $\hat{\mathbf{n}}_d = (n_{x,d}, n_{y,d}, n_{z,d})$ are the components of the unit vector.

Now, like the **Rotosolve** gates, we express the d -th gate as a $2^n \times 2^n$ matrix. We apply the tensor product of the unit 2×2 matrices to the d -th gate that acts on a particular qubit, hence

$$\begin{aligned}R'_{\hat{\mathbf{n}}_d}(\theta_d) &= I \otimes \dots \otimes I \otimes \left[\cos\left(\frac{\theta_d}{2}\right)I - i\sin\left(\frac{\theta_d}{2}\right)(\hat{\mathbf{n}} \cdot \boldsymbol{\sigma}) \right] \\ &\quad \otimes I \otimes \dots \otimes I.\end{aligned}\quad (15)$$

Applying the same procedure as in the previous section for **Rotosolve**, that is, we first apply Eq. (15) to Eq. (1). Here, we remark that we use ansatz circuit from Fig. 2. After that, a similar form of the cost function is obtained as in Eq. (6). Then, we define the quantum circuits that enter before and after the d -th gate as V_1 and V_2 , respectively. Here, the values of V_1 and V_2 depend on the values of $\hat{\mathbf{n}}_k$ and θ_k where $k \neq d$. Using the same definitions as in Eqs. (8) and (9), we arrive at the same form for the cost function as in Eq. (10)

$$\langle M \rangle_{\hat{\mathbf{n}}_d, \theta_d} = \text{Tr}\left(MR'_{\hat{\mathbf{n}}_d}(\theta_d)\rho R'_{\hat{\mathbf{n}}_d}(\theta_d)^\dagger\right).\quad (16)$$

The **Fraxis** is optimized using Lagrange multipliers to minimize the cost function $\langle M \rangle_{\hat{\mathbf{n}}_d, \theta_d}$ w.r.t. the axis unit vector $\hat{\mathbf{n}}$ [37]. We follow the notation from Ref. [37], where the subscript d is omitted to improve readability. We also set $\theta_d = \pi$ for the rest of the section.

First, we want to find the optimal parameters $\hat{\mathbf{n}}^*$ and Lagrange multiplier λ^* , which minimize the objective function

$$(\hat{\mathbf{n}}^*, \lambda^*) = \underset{\hat{\mathbf{n}}, \lambda}{\text{argmin}} f(\hat{\mathbf{n}}, \lambda),\quad (17)$$

where

$$f(\hat{\mathbf{n}}, \lambda) \equiv \langle M \rangle_{\hat{\mathbf{n}}} - \lambda(n_x^2 + n_y^2 + n_z^2 - 1).\quad (18)$$

Differentiating the objective function in Eq. (17) w.r.t. n_x, n_y and n_z yields the following set of equations [37]

$$\begin{aligned}\frac{\partial f}{\partial n_x} &= 2n_x \text{Tr}(MX\rho X) + n_y \text{Tr}(MX\rho Y + MY\rho X) \\ &\quad + n_z \text{Tr}(MX\rho Z + MZ\rho X) - 2\lambda n_x,\end{aligned}\quad (19)$$

$$\begin{aligned}\frac{\partial f}{\partial n_y} &= 2n_y \text{Tr}(MY\rho Y) + n_x \text{Tr}(MX\rho Y + MY\rho X) \\ &\quad + n_z \text{Tr}(MY\rho Z + MZ\rho Y) - 2\lambda n_y,\end{aligned}\quad (20)$$

$$\begin{aligned}\frac{\partial f}{\partial n_z} &= 2n_z \text{Tr}(MZ\rho Z) + n_x \text{Tr}(MX\rho Z + MZ\rho X) \\ &\quad + n_y \text{Tr}(MY\rho Z + MZ\rho Y) - 2\lambda n_z.\end{aligned}\quad (21)$$

The optimal $\hat{\mathbf{n}}^* = (n_x^*, n_y^*, n_z^*)^T$ satisfies the following condition

$$\frac{\partial f}{\partial n_x} = \frac{\partial f}{\partial n_y} = \frac{\partial f}{\partial n_z} = 0.\quad (22)$$

Furthermore, using the definitions from Ref. [37], we write the cross-term traces (i.e. $\text{Tr}(MX\rho Y)$) as follows

$$\text{Tr}(MX\rho Y + MY\rho X) = 2r_{(x+y)} - r_x - r_y,\quad (23)$$

$$\text{Tr}(MX\rho Z + MZ\rho X) = 2r_{(x+z)} - r_x - r_z,\quad (24)$$

$$\text{Tr}(MY\rho Z + MZ\rho Y) = 2r_{(y+z)} - r_y - r_z,\quad (25)$$

where $r_x, r_y, r_z, r_{(x+y)}, r_{(x+z)}$ and $r_{(y+z)}$ are defined as follows

$$r_x = \text{Tr}(MX\rho X),\quad (26)$$

$$r_y = \text{Tr}(MY\rho Y),\quad (27)$$

$$r_z = \text{Tr}(MZ\rho Z),\quad (28)$$

$$r_{(x+y)} = \text{Tr}\left(M\left(\frac{X+Y}{\sqrt{2}}\right)\rho\left(\frac{X+Y}{\sqrt{2}}\right)\right),\quad (29)$$

$$r_{(x+z)} = \text{Tr}\left(M\left(\frac{X+Z}{\sqrt{2}}\right)\rho\left(\frac{X+Z}{\sqrt{2}}\right)\right),\quad (30)$$

$$r_{(y+z)} = \text{Tr}\left(M\left(\frac{Y+Z}{\sqrt{2}}\right)\rho\left(\frac{Y+Z}{\sqrt{2}}\right)\right).\quad (31)$$

Finally, with these definitions, we can form the linear system of equations from Eqs. (19)–(21) and Eq. (22)

$$\begin{pmatrix} 2r_x & 2r_{(x+y)} - r_x - r_y \\ 2r_{(x+y)} - r_x - r_y & 2r_y \\ 2r_{(x+z)} - r_x - r_z & 2r_{(y+z)} - r_y - r_z \end{pmatrix} \begin{pmatrix} n_x^* \\ n_y^* \\ n_z^* \end{pmatrix} = 2\lambda^* \mathbf{I} \begin{pmatrix} n_x^* \\ n_y^* \\ n_z^* \end{pmatrix}. \quad (32)$$

Here, we remark that this represents the simplified Free-Axis Selection from Ref. [37], where the rotation angle θ_d is fixed to π .

After forming the matrix from the measurements in Eq. (32), the optimal axis is calculated by solving the three eigenvalues and eigenvectors in Eq. (32). The optimal axis $\hat{\mathbf{n}}^*$ is the eigenvector that corresponds to the lowest eigenvalue. The optimal value for λ^* is only solved when using the general version of Free-Axis Selection. For a comprehensive description, see Ref. [37].

D. Free Quaternion Selection Optimizer

Free Quaternion Selection (FQS) optimizer [38] is a matrix-diagonalization-based optimizer that optimizes a unit quaternion $\mathbf{q}_d = (q_0, q_1, q_2, q_3)$ rather than the unit axis $\hat{\mathbf{n}}$ as in the case of **Fraxis**. FQS expands the idea of **Fraxis** where we represent the single-qubit gate entirely in parameterized quaternion form. That is, instead of using the axis $\hat{\mathbf{n}}$, the identity element in Eq. (15) is also included. We start by expressing the unit axis $\hat{\mathbf{n}}$ in spherical coordinates as follows [38]

$$\hat{\mathbf{n}} = \hat{\mathbf{n}}(\psi, \varphi) = (\cos \psi, \sin \psi \cos \varphi, \sin \psi \sin \varphi), \quad (33)$$

where ψ is the polar angle and φ is the azimuth angle. Then, we define the extended Pauli matrix $\boldsymbol{\varsigma} \equiv (\varsigma_I, \varsigma_x, \varsigma_y, \varsigma_z) = (I, -iX, -iY, -iZ)$. Now we can express the single-qubit gate as [38, 39]

$$R'_{\hat{\mathbf{n}}_d(\psi, \varphi)}(\theta) = I \otimes \cdots \otimes I \otimes [\mathbf{q}_d(\theta, \psi, \varphi) \cdot \boldsymbol{\varsigma}] \\ \otimes I \otimes \cdots \otimes I \equiv R'(\mathbf{q}_d). \quad (34)$$

We remark that the subscript d has been dropped from the angular variables θ, ψ , and φ to clarify the notation.

We can now focus on the optimization of the single-qubit gate. The same procedure that we applied to **Rotosolve** and **Fraxis** also works on the FQS optimizer. Again, applying the Eq. (34) to Eq. (1) leads to Eq. (6). Then, define the quantum circuits before and after the d -th parameterized gate $R'(\mathbf{q}_d)$ as V_1 and V_2 , respectively. After that, using the cyclic property of the trace operation and definitions from Eqs. (8) and (9) we arrive at the quadratic form for the cost function $\langle M \rangle_{\mathbf{q}_d}$ as

$$\langle M \rangle_{\mathbf{q}_d} = \text{Tr}(MR'(\mathbf{q}_d)\rho R'(\mathbf{q}_d)^\dagger). \quad (35)$$

Since the components of a unit quaternion \mathbf{q} do not affect the matrix products, we focus on the terms $\text{Tr}(M\boldsymbol{\varsigma}'_d\rho\boldsymbol{\varsigma}'_d^\dagger)$. Here, we have used $\boldsymbol{\varsigma}' = I \otimes \cdots \otimes \boldsymbol{\varsigma} \otimes \cdots \otimes I$. We now construct the matrix $S = (S_{\mu\nu})$ which can be expressed as follows [38]

$$S_{\mu\nu} = \frac{1}{2} \text{Tr}[M(\boldsymbol{\varsigma}'_\mu\rho\boldsymbol{\varsigma}'_\nu^\dagger + \boldsymbol{\varsigma}'_\nu\rho\boldsymbol{\varsigma}'_\mu^\dagger)]. \quad (36)$$

The matrix S is a real 4×4 symmetric matrix with all real entries.

Thus, we obtain the quadratic form for the cost function in terms of \mathbf{q}_d

$$\langle M \rangle_{\mathbf{q}_d} = \mathbf{q}_d^T S \mathbf{q}_d. \quad (37)$$

Similarly to **Fraxis**, the unit quaternion \mathbf{q}_d is optimized by solving the eigenvectors and eigenvalues of the matrix S formed from the measured expectation values $\langle M \rangle$. The optimal \mathbf{q}_d^* is the eigenvector of S that corresponds to the lowest eigenvalue.

Next, we show how to implement our proposed gate freezing method for the **Rotosolve**, **Fraxis**, and FQS.

III. FREEZING THRESHOLD FOR THE PARAMETERS

In this section, we present our proposed gate freezing method for **Rotosolve**, **Fraxis**, and FQS. We start by considering a freezing threshold, which determines when the optimizable gates should be “frozen”. That is, we should not optimize the specific gates for κ iterations until we begin optimizing them again. To activate the gate freezing, we must first clearly define when this occurs. We use a freezing threshold T , which is a measure of how much we allow the gates parameter θ_k to change compared to the previous iteration. Here, the parameter θ_k may be multidimensional instead of a single scalar value, such as the parameters for **Fraxis** and FQS. We note that the parameters of **Fraxis**, $\hat{\mathbf{n}}_d$ can be represented as quaternions by setting the first component of the quaternion to zero as follows $\mathbf{q}_d = (0, n_{x,d}, n_{y,d}, n_{z,d})$. In this section, we use the quaternion representation for both **Fraxis** and FQS. The distance between the parameters is denoted by \mathcal{D} .

A. Gate Freeze with Parameter Values

We now introduce a freezing method based on the previous parameter values θ_k . The **Rotosolve** optimizer uses only a one-dimensional parameter, an angle θ_k for the given rotation gate R_k , where $R_k \in \{R_X, R_Y, R_Z\}$. When computing the distance between the previous and current parameters, we also need to take into account the cyclic boundary $(-\pi, \pi]$. That is, we define the distance between the parameters as follows

$$d_{\text{direct}}(\theta_{k,\text{prev}}, \theta_{k,\text{new}}) = |\theta_{k,\text{prev}} - \theta_{k,\text{new}}|. \quad (38)$$

Then, we need to ensure that the correct distance is chosen. The total distance of the interval is 2π . The dis-

tance is wrapped around the interval $(-\pi, \pi]$ by computing $d_{wrap} = 2\pi - d(\theta_{k,prev}, \theta_{k,new})$. Finally, we choose the smallest of these values as follows

$$\mathcal{D}(\theta_{k,prev}, \theta_{k,new}) = \min(d_{direct}, d_{wrap}). \quad (39)$$

The parameters of **Fraxis** and **FQS** optimizers can be represented on the unit sphere and hypersphere, respectively. On a spherical surface, the shortest distance is not Euclidean, but rather a great circle distance. That is, we cannot use the Euclidean distance $d_E(\mathbf{q}_{k,prev}, \mathbf{q}_{k,new}) = \|\mathbf{q}_{k,prev} - \mathbf{q}_{k,new}\|$ as a measure between the values of the previous and the new parameters. The great circle distance d_g for the n -dimensional unit sphere is computed as follows

$$d_g(\mathbf{q}_{k,prev}, \mathbf{q}_{k,new}) = \arccos(\mathbf{q}_{k,prev} \cdot \mathbf{q}_{k,new}). \quad (40)$$

When evaluating the expectation value of the form $\langle M \rangle = \text{Tr}(MU\rho U^\dagger)$, we need to take into account that the transformation $U \rightarrow -U$ produces the same expectation value $\langle M \rangle$. This corresponds to mapping the axis of rotation on the opposite side of the (hyper)sphere. When we compute the great circle distance between the new and old parameters, we also need to compute the distance from the opposite side of the sphere to the new point. The great circle distance between the opposite axes on the unit sphere is π , so we need to compute the minimum of these two distances. Similarly to **Rotosolve**, we wrap the distance $d_{wrap} = \pi - d_g(\mathbf{q}_{k,prev}, \mathbf{q}_{k,new})$. Then we choose a smaller value of these two as follows

$$\mathcal{D}(\mathbf{q}_{k,prev}, \mathbf{q}_{k,new}) = \min(d_g, d_{wrap}). \quad (41)$$

This works for both **Fraxis** and **FQS** optimizer parameters. Next, we implement gate freezing by evaluating a matrix norm that determines whether a gate should be frozen.

B. Gate freezing with matrix norms

Now we implement a more generalized approach to gate freezing. Each single-qubit gate is a unitary matrix that acts on the given qubit. These unitaries correspond to a rotation on a Bloch sphere. Suppose we have unitary matrices U and V , representing the gate before and after optimization, respectively, where $U, V \in SU(2)$. To quantify how much a gate changes in each optimization step, we use the Frobenius norm $\|U - V\|_F$, which provides a matrix-level distance between the two gates. The Frobenius norm is defined as

$$\|U - V\|_F = \sqrt{\text{Tr}[(U - V)^\dagger(U - V)]}. \quad (42)$$

We remark that in this work, we focus on single-qubit gates, which are 2×2 unitary matrices. However, this approach can be naturally extended to arbitrary n -qubit gates, as it is not limited by specific gate parameters,

unlike the approach discussed in Sec. III A. In the context of unitary 2×2 matrices, the expression simplifies to

$$\|U - V\|_F = \sqrt{4 - 2 \cdot \text{Re}(\text{Tr}(U^\dagger V))}, \quad (43)$$

using the fact that $\text{Tr}(U^\dagger U) = \text{Tr}(V^\dagger V) = \text{Tr}(I) = 2$ for 2×2 unitary matrices U and V . Since any global phase factor of V does not influence the physical state, we can multiply V by a complex phase $e^{i\delta}$ without altering observable outcomes. We exploit this degree of freedom to rotate the complex phase of the Frobenius inner product $\text{Tr}(U^\dagger V)$ onto the positive real axis. Specifically, we select δ such that

$$\text{Tr}(U^\dagger e^{i\delta} V) = e^{i\delta} \text{Tr}(U^\dagger V) = |\text{Tr}(U^\dagger V)|. \quad (44)$$

Having forced the overlap to be a non-negative real number, its magnitude is now as large as possible. Thus, we derive the following expression for the distance between unitary matrices on the Bloch sphere:

$$\mathcal{D}(U, V) = \sqrt{4 - 2 \cdot |\text{Tr}(U^\dagger V)|}. \quad (45)$$

Finally, we normalize this matrix norm distance to be strictly in the range $[0, 1]$. The expression inside the square root achieves its maximum value when $\text{Tr}(U^\dagger V) = 0$. Therefore, we normalize the Frobenius norm by dividing by a factor of 2, resulting in the normalized distance. Other matrix norms, such as the spectral norm, can also be used to measure the distance between given matrices U and V . In this work, we employ the above formulation in our results. Additionally, this method can be extended to any n -qubit gates, where $n \geq 2$. Then we would need to compute the matrix norms for the $2^n \times 2^n$ matrices. We provide additional formulation for n -qubit gates in Appendix E. The gate freezing algorithm is described in Algorithm 1, which can use any distance metric \mathcal{D} .

C. Incremental increase to freezing iterations

Now that we have created algorithm-specific gate freezing algorithms, we also introduce an algorithm that tunes the freezing iteration hyperparameter κ during optimization. Before starting optimization, we initialize a gate freezing iteration vector $\boldsymbol{\kappa}$ of optimizable parameters of length, where each element κ_d is set to one. During optimization, if the d -th gate is frozen, then we increment the freezing iteration vector element κ_d by one. This means that the next time the d -th gate is frozen, it has a longer freezing time by one iteration. That is, every time any gate is frozen, its freezing time increases linearly. The heuristic behind this idea is to increasingly penalize the optimization of gates that consecutively exceed the freezing threshold, leading to more optimizations of poorly optimized gates.

We define the incremental increase of the freezing iteration in the Algorithm 2. The algorithm needs a specific

Algorithm1 Gate freezing method for VQAs

```

1: Inputs: A Variational Quantum Circuit  $U$  with fixed architecture, Hermitian measurement operator as the cost function, heuristically selected stopping criterion, distance metric  $\mathcal{D}$ , and an optimizer (e.g. Rotosolve).
2: Initialize gate freeze iterations  $\kappa \in \mathbb{Z}_+$ 
3: Initialize the parameters,  $\theta_d$  for  $d = 0, \dots, Ln - 1$  heuristically or at random.
4: Initialize a fixed freezing threshold  $T$ .
5: repeat
6:   for  $d = 0, \dots, Ln - 1$  do
7:     if  $d$ -th gate is not frozen then
8:       Fix all gates except the  $d$ -th one
9:       Optimize the  $d$ -th gate  $U_d$  with given optimizer.
10:      Compute  $\Delta U_d \leftarrow \mathcal{D}(U_{d,prev}, U_{d,new})$ 
11:      if  $\Delta U_d < T$  then
12:        Freeze  $d$ -th gate for  $\kappa$  iterations
13:      end if
14:    end if
15:  end for
16: until stopping criterion is met

```

distance metric \mathcal{D} and a threshold T for the given optimizer.

Algorithm2 Incremental increase to freezing iterations for VQAs

```

1: Inputs: A Variational Quantum Circuit  $U$  with fixed architecture, Hermitian measurement operator as the cost function, heuristically selected stopping criterion, a distance metric  $\mathcal{D}$ , and an optimizer (e.g. Rotosolve).
2: Initialize the parameters,  $\theta_d$  for  $d = 0, \dots, Ln - 1$  heuristically or at random.
3: Initialize gate freeze iterations vector  $\kappa$ , where  $\kappa_d = 1$  for  $d = 0, \dots, Ln - 1$ .
4: Initialize a fixed freezing threshold  $T$ .
5: repeat
6:   for  $d = 0, \dots, Ln - 1$  do
7:     if  $d$ -th gate is not frozen then
8:       Fix all gates except the  $d$ -th one
9:       Optimize the  $d$ -th gate  $U_d$  with given optimizer.
10:      Compute  $\Delta U_d \leftarrow \mathcal{D}(U_{d,prev}, U_{d,new})$ 
11:      if  $\Delta U_d < T$  then
12:        Freeze  $d$ -th gate for  $\kappa_d$  iterations
13:         $\kappa_d \leftarrow \kappa_d + 1$ 
14:      end if
15:    end if
16:  end for
17: until stopping criterion is met

```

IV. RESULTS

In this section, we examine the results of our proposed method compared to the regular versions of the covered optimizers, where gate freezing is not applied at all. First, we go through the results for the 5-qubit Heisenberg Hamiltonian in a one-dimensional lattice with periodic boundary conditions. This was done for all opti-

mizers. After that, we show results with the incremental gate freeze iterations for all optimizers and the individual gate freezing amounts for the whole ansatz circuit.

Furthermore, we applied incremental gate freezing for the Fermi-Hubbard model with a 6-qubit system on the 1×3 lattice.

For the last experiment, we tested the scalability of our method across the number of qubits for the Heisenberg model with **Rotosolve** optimizer. We used 5 to 15 qubits and set the number of layers $L = \mathcal{O}(n)$ for different numbers of qubits.

In all experiments, we used the ansatz circuit from Fig. 3 for **Rotosolve** and the ansatz circuit from Fig. 2 for **Fraxis** and **FQS**. The gates in the circuits were optimized sequentially, layer by layer. We start from the top left of the circuit and then move down in the circuit to the next qubit gate after optimizing the first gate. The optimization sequence in one layer is shown in Figs. 2 and 3. After optimizing all the gates in one layer, we move on to the next layer. This process is continued until all gates in the circuit are optimized. We define this as one iteration. The regular versions of the optimizers' stopping criterion are set to 50 iterations for the **Rotosolve**, 50 iterations for **Fraxis**, and 30 for **FQS**. This gives the total number of gate optimizations in one run, which is the number of iterations times the number of gates in the circuit. The gate freezing method algorithms, on the other hand, optimize the circuit until the set amount of these gate optimizations is reached to get comparable results with the regular optimizers.

The parameters for all optimizers are initialized uniformly. The parameters θ_d for the **Rotosolve** are sampled from the uniform distribution $(-\pi, \pi]$, the **Fraxis** parameters, unit axis \hat{n}_d , from the uniform spherical distribution and the parameters of **FQS**, the unit quaternions q_d , from the uniform spherical distribution in four dimensions.

We tested the performance of the gate freezing method, where in all experiments the threshold T was set to one of the following values: $T = 0.01, 0.005, 0.001$. We choose these threshold values heuristically by examining how the parameters of individual gates change over time in one run and the proportion of gates in PQC that exceed the freezing threshold T . The change in parameter values over the iterations is illustrated in Fig. 4. We observed a similar behavior for both parameter-based and matrix norm metrics with **Fraxis** and **FQS** optimizers. Also, the behavior was similar to the Fermi-Hubbard Hamiltonian for all optimizers and metrics. Figure 5 illustrates the percentage of gates exceeding the threshold T , using the parameter-based metric to compute the distance between new and previous parameter values. Here, we used a 5-qubit Heisenberg Hamiltonian with 3 layers for **Rotosolve** and 5 layers for **Fraxis** and **FQS**, respectively. With $T = 0.01$ and 0.005 , at the end of the optimization, all gates in PQC exceed the threshold value for **Rotosolve** and **Fraxis**. For **FQS** optimizer, the percentage of gates exceeding T plateaus around 80%. Since we

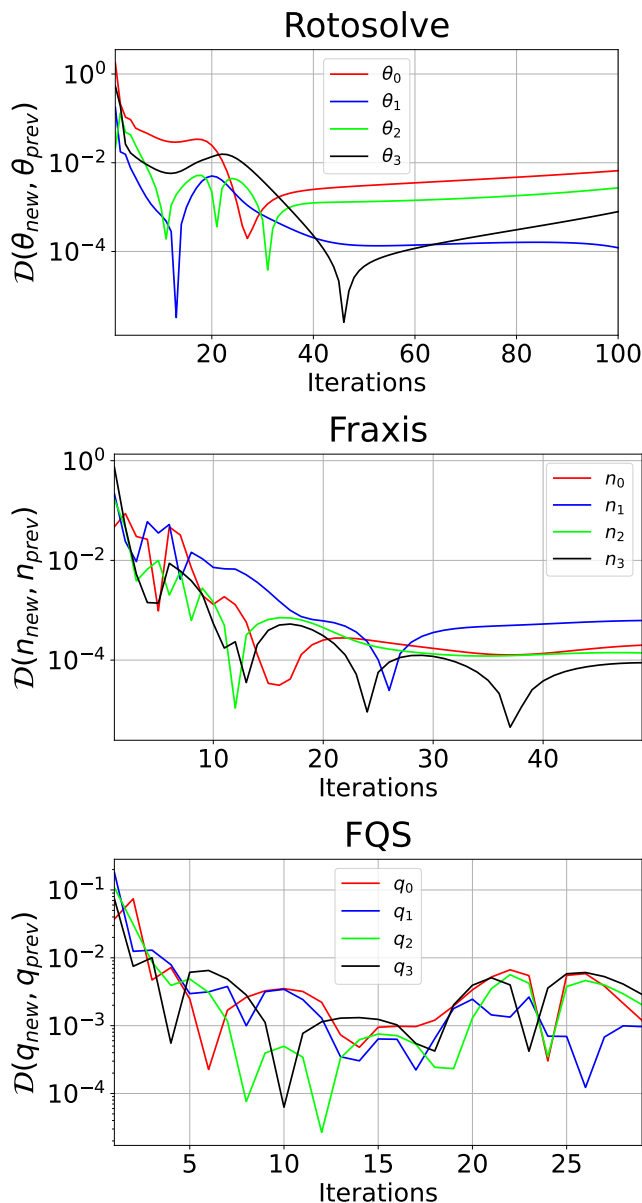


FIG. 4: Distance between previous and new parameter values over iterations for **Rotosolve**, **Fraxis**, and **FQS** optimizers. Each line corresponds randomly chosen parameter in the PQC of one run. The vertical axis is the parameter-based distance from Sec. III A on a logarithmic scale.

used 5 layers, this means that one layer of gates does not exceed the freezing threshold value at all for any value of T . This is further explored in Sec. IV A 3. In summary, the parameters of the first layer are rarely frozen when using the FQS optimizer, which explains the plateauing in Fig. 5. For $T = 0.001$, all gates in PQC optimized by **Fraxis** exceed the threshold, but it takes more iterations to reach that point than other values of T . **Rotosolve** and **FQS**, on the other hand, do not reach a fully frozen circuit as **Fraxis** when we set $T = 0.001$.

In this work, we used the PennyLane package version 0.40 [42], and Python version 3.11. to generate the data for the plots.

A. Heisenberg Model

Next, we present results of the proposed methods for the 5-qubit cyclic one-dimensional Heisenberg model [43]. The corresponding Hamiltonian is defined as

$$H = J \sum_{i=1}^n (X_i X_{i+1} + Y_i Y_{i+1} + Z_i Z_{i+1}) + h \sum_{i=1}^n Z_i, \quad (46)$$

where J is the strength of the spin interaction and h is the magnetic field strength along the Z-axis. We set $J = h = 1$ in this work.

The values for the freeze iteration parameter were set to $\kappa = 5, 10, 15$ for **Rotosolve**. For **Fraxis** and **FQS**, lower values were used due to a good convergence of these algorithms w.r.t. the number of gate optimizations. That is, we set $\kappa = 2, 5$ for **Fraxis** and **FQS**. In all experiments, 20 runs were carried out for each iteration value of the freeze κ and threshold T , as well as the regular versions of the algorithms, which act as a reference to compare how well the gate freezing works. Each run consists of a total of 50 iterations for **Rotosolve**, 50 for **Fraxis**, and 30 for **FQS**. The same experiments were repeated for the incremental increase to the freezing iteration algorithm for all optimizers. We also examine what values the gate freeze iteration vector κ has after optimizing for each gate κ_d with different values of T using Algorithm 2. In all the following figures in this subsection, each line in the top row represents a median of 20 runs. In the bottom row, the box plots summarize the results at the end of 20 runs. The boxes span from the first quartile (Q1) to the third quartile (Q3); horizontal bar within each box indicates the median, the diamond marker denotes the mean, and the whiskers represent values within 1.5 times the interquartile range (IQR). The ground state of the Hamiltonian is approximately $E_g = -8.47$.

We provide additional results for incremental gate freeze method in Appendix B and with different ansatz circuits in Appendix C.

1. Parameter Distances

The results for gate freezing with iterations $\kappa = 5, 10, 15$ and incremental gate freezing with **Rotosolve** are shown in Fig. 6. In both subplots in Fig. 6, the gate freezing method outperforms the original base **Rotosolve** in terms of convergence speed and better mean values across the 20 runs. For all freeze iterations κ , the best median value in each case was $T = 0.001$. This outcome was also observed for the incremental freezing method. Subsequently, the next most effective freezing threshold was $T = 0.005$ across different values of κ . However, for

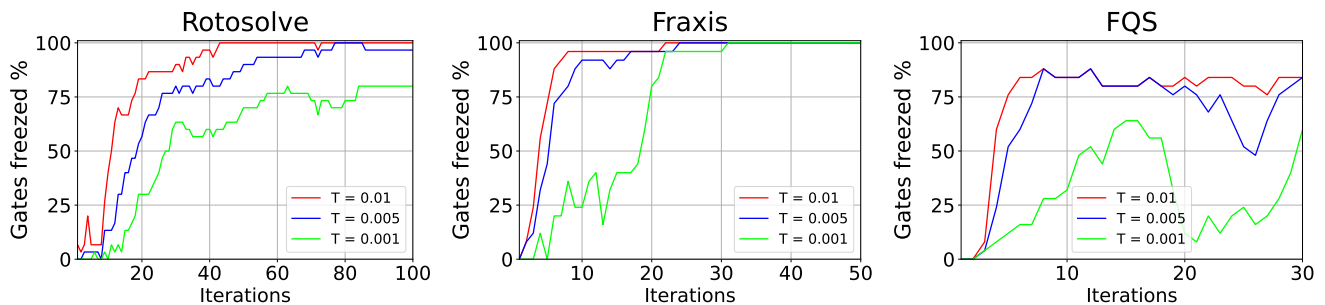


FIG. 5: The proportion of gates in PQC exceeding the freezing threshold T over iterations for **Rotosolve**, **Fraxis**, and **FQS** optimizers. Each line corresponds to the percentage (%) of gates exceeding the threshold T in the PQC of one run. Threshold values T were set to $T = 0.01$ (red), 0.005 (blue), and 0.001 (green), and a parameter-based metric was used.

the incremental freezing method, a threshold $T = 0.01$ yielded better performance. In all experiments, the regular **Rotosolve** without gate freezing had the worst performance of all.

For the **Fraxis** algorithm, we obtained similar results as for the **Rotosolve** algorithm. For **Fraxis** we used one optimizable gate for each qubit in a layer instead of the pair gates for the ansatz circuit shown in Fig. 3. Otherwise, the structure stays the same. The results are fully shown in Fig. 7, where we used 5 layers with 5 qubits and the freeze iterations κ were set to $\kappa = 2$ and 5 in each subplot, respectively. The results also include the incremental gate freezing method in its subplot. In subplots for $\kappa = 2$ and $\kappa = 5$, the median for regular **Fraxis** is larger compared to its gate freezing counterparts. For incremental gate freezing, the median is higher, and the best performer is $T = 0.001$. Like for **Rotosolve** in all subplots, the lowest threshold value $T = 0.001$ is the best, and for specific freeze iterations κ it is $T = 0.005$. However, for incremental freezing, the threshold $T = 0.01$ is second best, followed by $T = 0.005$. Again, the regular **Fraxis** performed the worst compared to the gate freezing methods.

For the **FQS**, we employed a 5-qubit system and 5 layers, freezing iterations $\kappa = 2$ and 5 , incremental gate freezing, as well as the same ansatz circuit used with the **Fraxis** algorithm. The results for **FQS** are shown in Fig. 8. In contrast to the results for **Rotosolve** and **Fraxis**, the base version of **FQS** performs the best in this case. Conversely, the relative performance of the gate freezing methods for κ iterations remains the same. The best gate freezing threshold is $T = 0.001$, followed by 0.005 and 0.01 . The best threshold for incremental freezing is $T = 0.005$, followed by 0.001 , and finally 0.01 .

It appears that the more expressive the optimizer is, the less advantage the gate freezing provides compared to its base version. Next, we show our results for the matrix norm as a distance measure.

2. Matrix Norm Distances

In this section, we use the derived matrix norm from Sec. III B to measure the rotations of the unitaries on a Bloch sphere. Due to the simple nature of **Rotosolve**, we now only consider **Fraxis** and **FQS**. Similarly to the previous section, we use $\kappa = 2, 5$ and incremental freezing for gate freezing. The threshold values T are set to $0.01, 0.005$, and 0.001 . All runs were carried out with 50 iterations for each run for **Fraxis** and 30 iterations for **FQS**. The ansatz circuit in Fig. 3 with 5 layers and qubits was used for both optimizers.

Next, present the results in Fig. 10 for **Fraxis** optimizer. The results are almost identical when the great circle distance is used between the new and old parameters, derived in Sec. III A. The overall threshold value $T = 0.001$ is the best performer. Now, the convergence of the median is somewhat slower compared to the parameter distance case.

Finally, we show the results for **FQS** optimizer using the matrix norm as a metric. Similarly to the **Fraxis** case, the results resemble those observed in the parameter distance case. Here, for the incremental freezing method, the median value at $T = 0.001$ has the fastest initial convergence, but the worst overall value after the optimization process. The best performer is the base version of **FQS**, followed by $T = 0.01$ and then 0.005 . Again, the results favor using the base version of **FQS**.

3. Incremental freezing – Gate freeze iterations

In this section, we show our results for individual gates w.r.t. the number of gate freeze iterations κ_d . We examine the average of the incremental gate freezing iterations κ that exceeded the given threshold T . After each run, the vector κ was saved in the data file. We ran a total of 50 runs for each optimizer with the same number of iterations as mentioned at the beginning of Sec. IV. After that, we take the mean of the gate freezing iterations for each κ_d and plot the results as a two-dimensional grid,

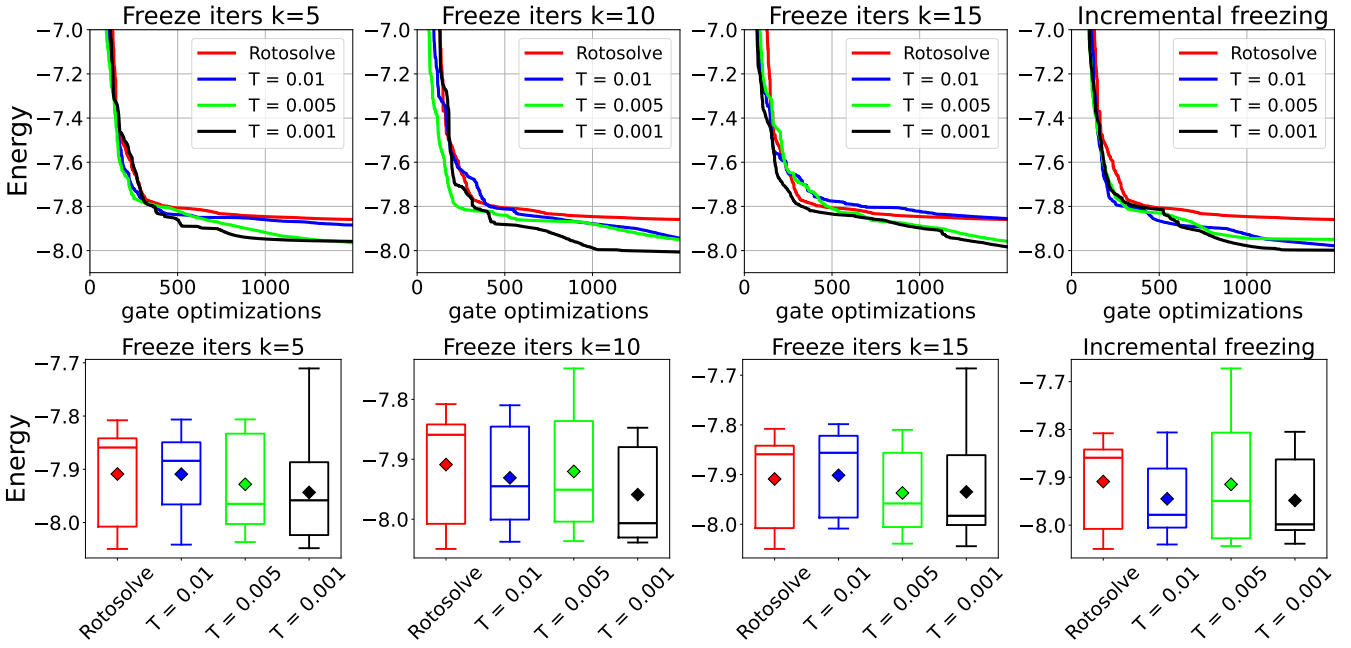


FIG. 6: Results for 5-qubit Heisenberg model with regular Rotosolve (red) and with the parameter gate freezing method for 3 layers. Gate freezing threshold was set to $T = 0.01$ (blue), 0.005 (green), 0.001 (black). Freeze iterations $\kappa = 5, 10, 15$ and incremental gate freezing were used.

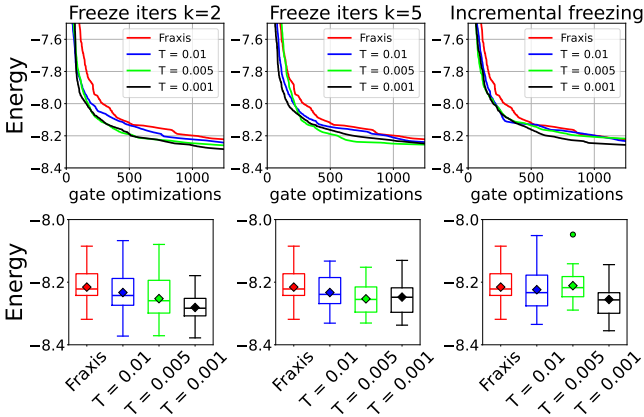


FIG. 7: Results for 5-qubit Heisenberg model with regular Fraxis (red) and with the parameter gate freezing method for 5 layers. Gate freezing threshold was set to $T = 0.01$ (blue), 0.005 (green), 0.001 (black). Freeze iterations $\kappa = 2, 5$ and incremental gate freezing were used.

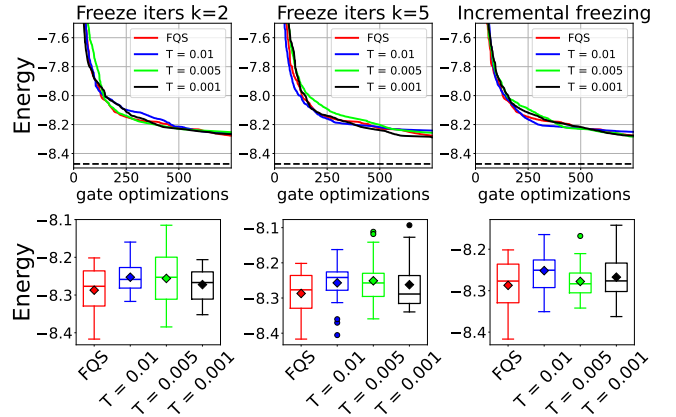


FIG. 8: Results for 5-qubit Heisenberg model with regular FQS (red) and with the parameter gate freezing method for 5 layers. Gate freezing threshold was set to $T = 0.01$ (blue), 0.005 (green), 0.001 (black). Freeze iterations $\kappa = 2, 5$ and incremental gate freezing were used.

where rows indicate the qubit index of the algorithm and a layer index indicating the layer to which the parameter belongs. The grid can be interpreted as representing the positions of the parameters in the circuit. That is, the leftmost column corresponds to the first gates optimized during each iteration, while the rightmost column represents the last gates optimized in the circuit. The columns can be thought of as parameter layers in a QQC. Each

block in the grid represents the mean of the gate freeze iterations of 50 runs. Red cells indicate higher averages, while blue cells correspond to lower averages. For all optimizers, the angle distance between the parameters was used as a metric.

We show the results for Rotosolve in Fig. 11. Here, we have run a total of 50 runs with 3 layers. In the plots, there are a total of six columns, corresponding to one cir-

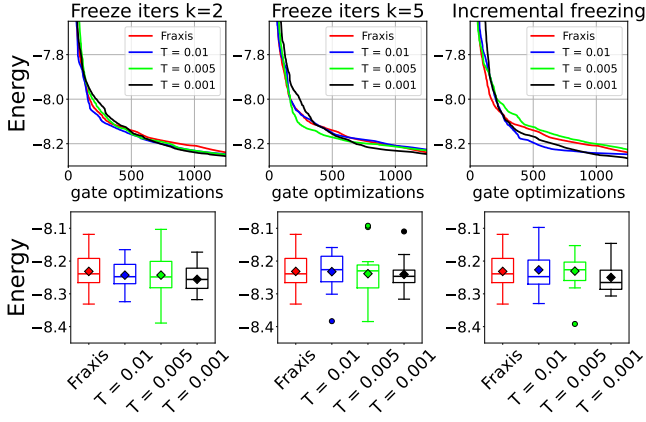


FIG. 9: Results for 5-qubit Heisenberg model with regular **Fraxis** (red) and with the matrix norm gate freezing method for 5 layers. Gate freezing threshold was set to $T = 0.01$ (blue), 0.005 (green), 0.001 (black). Freeze iterations $\kappa = 2, 5$ and incremental gate freezing were used.

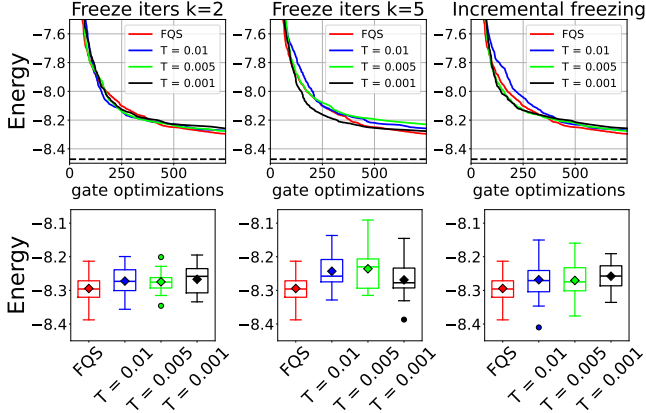


FIG. 10: Results for 5-qubit Heisenberg model with regular **FQS** (red) and with the matrix norm gate freezing method for 5 layers. Gate freezing threshold was set to $T = 0.01$ (blue), 0.005 (green), 0.001 (black). Freeze iterations $\kappa = 2, 5$ and incremental gate freezing were used.

circuit ansatz layer consisting of R_X and R_Y gates applied to each qubit. This increases the number of parameters in the circuit by twice the number of actual layers. The color of the grid squares is the average gate freeze iteration parameter κ_d for each gate over the 50 runs. The red color means a higher κ_d and blue a lower κ_d average value. That is, the red grid squares have been frozen more often and for longer during optimization than the blue grid squares.

In Fig. 11, we see that the lower the threshold value T , the more the gate freezing is focused on the last layer. This means that it is advantageous to focus on freezing these last few layers and/or gates in them. A peculiarly curious finding is that the most frozen gate is in

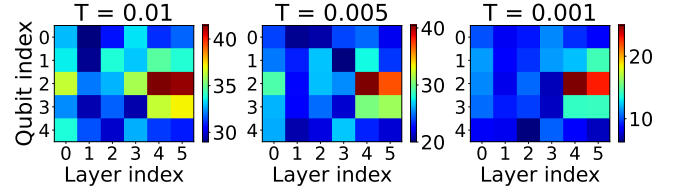


FIG. 11: Results for 5-qubit Heisenberg model with the incremental gate freezing method for 3 layers with **Rotosolve** algorithm. The gate freezing threshold T was set to have values $T = 0.01$ (left), 0.005 (mid) and 0.001 (right).

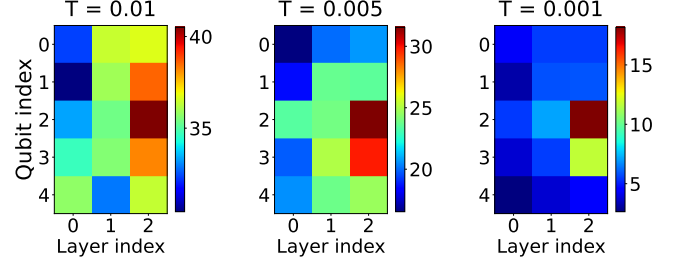


FIG. 12: Results for 5-qubit Heisenberg model with the incremental gate freezing method for 3 layers with **Fraxis** algorithm. A parameter-based freezing method was used, and the gate freezing threshold T was set to have values $T = 0.01$ (left), 0.005 (mid), and 0.001 (right).

the middle qubits gates in the last layer. They have a significantly higher average of gate freeze iterations κ_d compared to any other gate in the circuit. We remark that in each subplot, the color scale values are relative to its own subplot.

We repeated the same experiment on **Fraxis** with 3 layers and 50 runs. The results are shown in Fig. 12. As in the case of **Rotosolve**, we see similar results that with a lower threshold, the last layer in the optimization has proportionally larger freezing iterations compared to

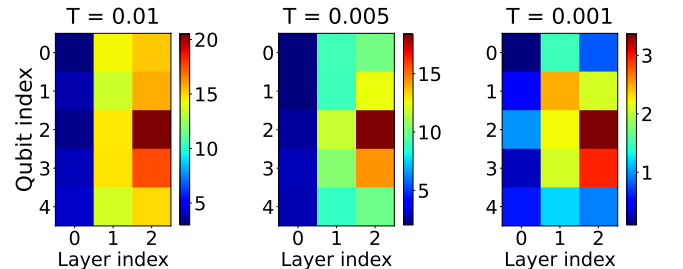


FIG. 13: Results for 5-qubit Heisenberg model with the incremental gate freezing method for 3 layers with **FQS** algorithm. A parameter-based freezing method was used, and the gate freezing threshold T was set to have values $T = 0.01$ (left), 0.005 (mid) and 0.001 (right).

earlier layers. We also notice the same behavior for the last row in all subplots of Fig. 12 as in Fig. 11. Again, the last layer obtains the highest average of the freezing iterations, and the middle qubit has the highest average of all. In all values of T , the gates of the first layer of the circuit, on average, are less frequently frozen.

Finally, we show our results for the FQS algorithm in Fig. 13. In all subplots, the first layer gates are rarely frozen compared to the rest. Again, we observe that, in most cases, the freezing focuses on the gates in the last layer—especially the middle-qubit gate in the last layer, as in the *Fraxis*' case. Overall, the results for FQS and *Fraxis* do not differ significantly.

In addition, we provide more results to this subsection in the Appendices B and C. In Appendix B, we examine the average of the incremental gate freezing iterations κ without applying the gate freezing at all for *Fraxis* and FQS with the parameter distance metric. In Appendix C, we conduct the same experiment as in this subsection but with the parameter distance metric for all optimizers and with different ansatz circuits that are provided in Appendix A.

In Appendix C, we provide additional results for various ansatz circuits, highlighting that the observed heat maps depend significantly on the choice of the ansatz. Furthermore, in Appendix D, we examine the mutual information between different qubits for each ansatz considered. By comparing the heat maps generated from mutual information and parameter gate freezing, we find that similar mutual information patterns across different ansatz circuits correspond closely to similar gate-freezing patterns. Thus, the average mutual information between qubits within the ansatz circuits helps explain the observed similarities in gate freeze heat maps.

B. Fermi-Hubbard Model

In this section, we show our results for the Fermi-Hubbard model [44], which describes how fermions interact in a lattice. The model is used to study the electronic and magnetic properties of materials, as well as in experiments with a fermionic quantum gas in the optical lattice [45]. We intend to solve the ground state of this model for a 1×3 lattice with a 6-qubit system. The Fermi-Hubbard model Hamiltonian is defined as follows [46].

$$H = -t \sum_{\langle i,j \rangle, \sigma} (\hat{c}_{i,\sigma}^\dagger \hat{c}_{j,\sigma} + \text{h.c.}) + U \sum_i \hat{n}_{i,\uparrow} \hat{n}_{i,\downarrow}. \quad (47)$$

Here, the first term denotes the kinetic term, t is the tunneling matrix, and $\langle i, j \rangle$ are the neighboring sites. The operators $\hat{c}_{i,\sigma}^\dagger$ and $\hat{c}_{j,\sigma}$ are the fermionic creation and annihilation operators, respectively, and h.c. stands for the hermitian conjugate. The operators $\hat{c}_{i,\sigma}^\dagger$ and $\hat{c}_{i,\sigma}$ correspond to adding or removing the fermion from the site i with the spin state σ . The final term is the potential term, where U is the strength of the interaction

on site and the occupation number \hat{n}_i is the number of particles on site i with up- or down states. In this work, set $t = U = 0.5$ in all experiments. The corresponding Hamiltonian is extracted using the PennyLane package [42] with the corresponding lattice size and coefficients t and U , and applying the Jordan-Wigner mapping [47] to the creation and annihilation operators. The mapping requires 2 qubits for each lattice site, which means that the lattice of size 1×3 is a 6-qubit system.

Next, we show our results for incremental freezing for *Rotosolve*, *Fraxis*, and FQS. In all the following figures in this subsection, each line in the top row represents a median of 20 runs. In the bottom row, the box plots summarize the results at the end of 20 runs. The boxes span from the first quartile (Q1) to the third quartile (Q3); horizontal bar within each box indicates the median, the diamond marker denotes the mean, and the whiskers represent values within 1.5 times the interquartile range (IQR). The ground state of the Hamiltonian is approximately $E_g = -1.25$.

1. Parameter Distances

We tested fixed and incremental freezing for *Rotosolve* with 3 layers and *Fraxis* and FQS optimizers with 5 layers. We used the same ansatz circuit as for the Heisenberg model. A total of 20 runs were performed. The number of gate optimization iterations was set to 50 for regular *Rotosolve* and *Fraxis*, and 30 for FQS. The incremental gate freezing algorithms were executed until they reached a total number of gate iterations equal to that of one run of the regular version of the corresponding algorithm.

The results for *Rotosolve* are shown in Fig. 14. For fixed freeze iterations $\kappa = 5$, the best convergence is achieved with $T = 0.005$ in terms of median and mean across the 20 runs. The runs of the base version of *Rotosolve* are tightly packed around the value -0.8 , but there are also several outliers, one value lies below -0.9 , and 3 values exceed the upper range of the whiskers. The other have larger inter-quartile ranges (box sizes) and no outliers except for the threshold $T = 0.001$. With freeze iterations $\kappa = 10$ and $\kappa = 15$, the convergence is slower, but the median values for the base version and freezing thresholds. Interestingly, the incremental gate freezing has approximately the same median value as the base version, regardless of the threshold value T .

We present the results for *Fraxis* optimizer in Fig. 15. For freeze iterations $\kappa = 2$, the best threshold value is $T = 0.005$. The values $T = 0.01$ and $T = 0.001$ have equivalent performance in terms of convergence speed and box plots. However, the threshold $T = 0.005$ is closer to the ground state of the Hamiltonian and best convergence. For freeze iterations $\kappa = 5$, the results are a bit worse for the gate freezing method than with $\kappa = 2$. The threshold value $T = 0.001$ is the best, followed by $T = 0.005$, then $T = 0.01$, and finally the base version

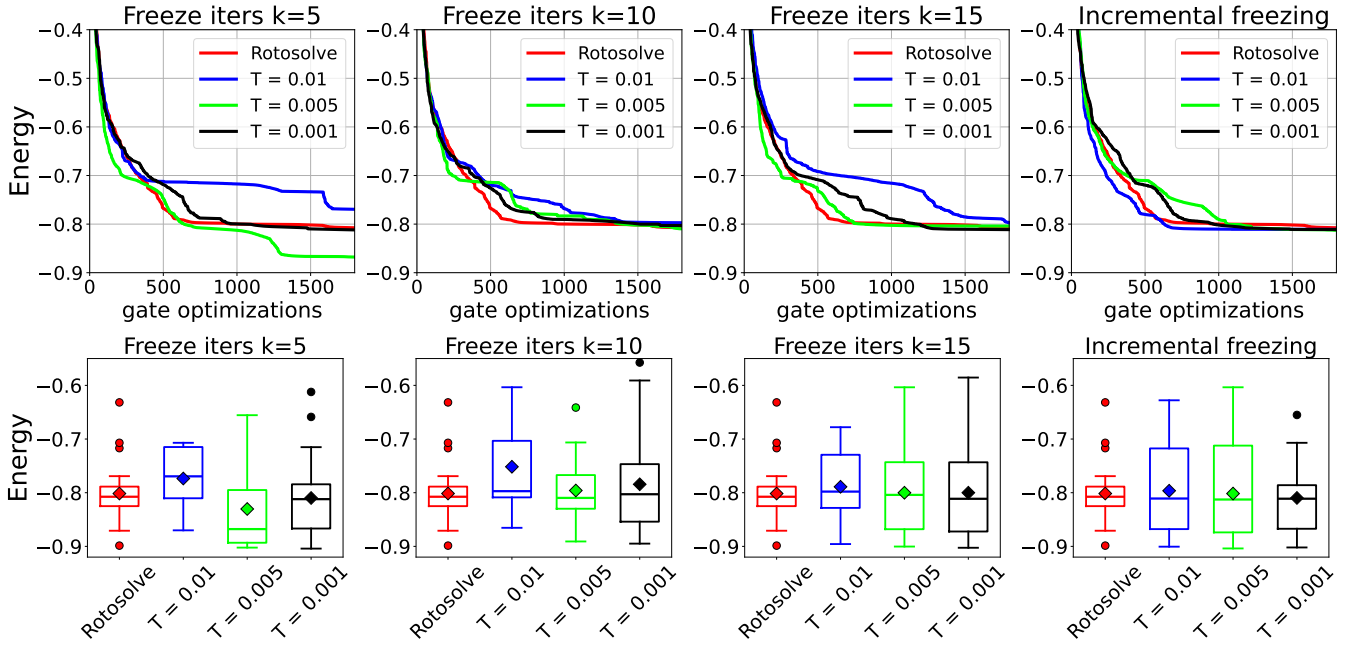


FIG. 14: Results for 6-qubit Fermi-Hubbard model with regular **Rotosolve** (red) and with the parameter gate freezing method for 3 layers. Gate freezing threshold was set to $T = 0.01$ (blue), 0.005 (green), 0.001 (black). Freeze iterations $\kappa = 5, 10, 15$ and incremental gate freezing were used.

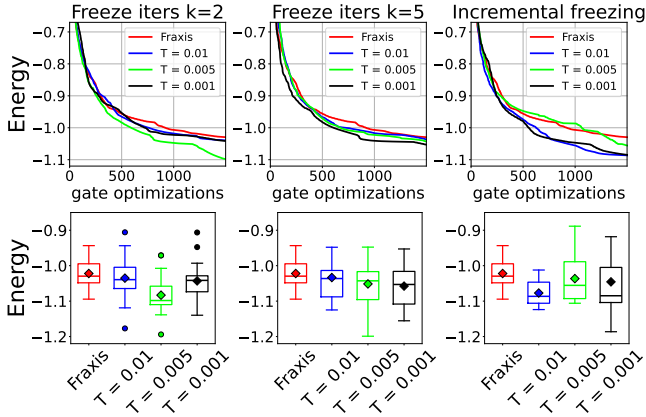


FIG. 15: Results for 6-qubit Fermi-Hubbard model with regular **Fraxis** (red) and with the parameter gate freezing method for 5 layers. Gate freezing threshold was set to $T = 0.01$ (blue), 0.005 (green), 0.001 (black). Freeze iterations $\kappa = 2, 5$ and incremental gate freezing were used.

of **Fraxis**, respectively. Although the median is slightly worse, the case with $T = 0.005$ has a range closer to the ground state than **Fraxis**. Incremental freezing also achieves faster median convergence for $T = 0.001$ and $T = 0.01$. The threshold value $T = 0.005$ comes right after, and the base version of the **Fraxis** is last.

Finally, we show the results for **FQS** optimizer in Fig. 16. For fixed gate iterations $\kappa = 2$ and $\kappa = 5$, the

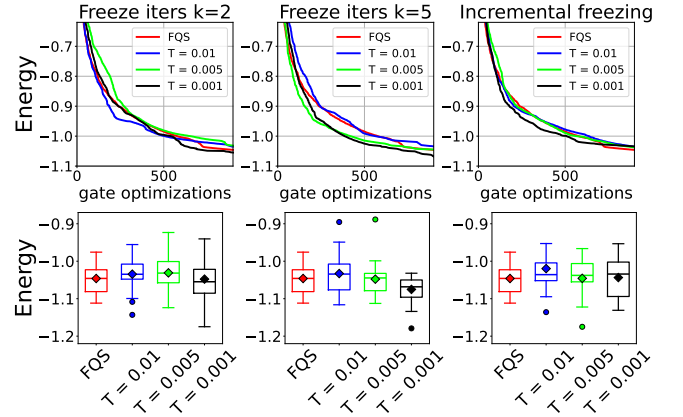


FIG. 16: Results for 6-qubit Fermi-Hubbard model with regular **FQS** (red) and with the parameter gate freezing method for 5 layers. Gate freezing threshold was set to $T = 0.01$ (blue), 0.005 (green), 0.001 (black). Freeze iterations $\kappa = 2, 5$ and incremental gate freezing were used.

threshold $T = 0.001$ yields the best median performance, and for $\kappa = 5$, it also results in the best convergence compared to the baseline. A similar trend is observed with incremental freezing, though only in terms of median convergence, not the final result. In contrast, when using fixed iteration freezing, lower threshold values generally lead to better overall results.

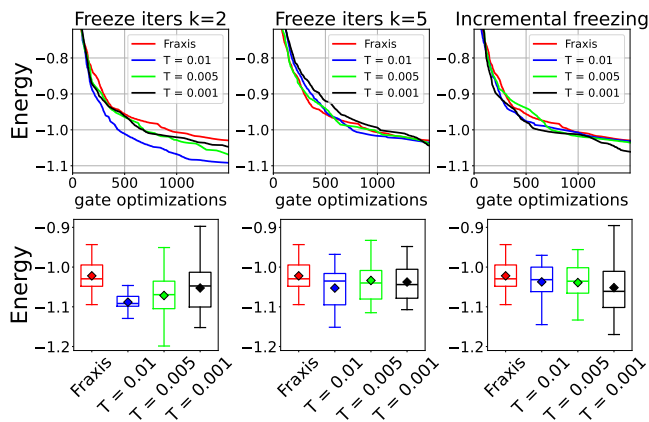


FIG. 17: Results for 6-qubit Fermi-Hubbard model with regular **Fraxis** (red) and with the matrix norm gate freezing method for 5 layers. Gate freezing threshold was set to $T = 0.01$ (blue), 0.005 (green), 0.001 (black). Freeze iterations $\kappa = 2, 5$ and incremental gate freezing were used.

2. Matrix Norm Distances

Now we present our results for **Fraxis** and **FQS** with matrix norm as distance metric. The experiment was done in the same way as for the parameter distances. A total of 20 runs with 50 iterations for **Fraxis** and 30 iterations for **FQS** with freeze iterations set to $\kappa = 2, 5$. The incremental gate freezing algorithms were executed until they reached a total number of gate iterations equal to that of one run of the regular version of the corresponding algorithm. In all gate freezing scenarios, we used the thresholds $T = 0.01, 0.005$, and 0.001 .

The results for **Fraxis** with matrix norm are shown in Fig. 17. When the fixed gate freezing iterations are set to $\kappa = 2$, we obtain the best overall results compared to $\kappa = 5$ and incremental freezing. Regardless of the threshold value T , the median converges faster than the base version of **Fraxis**. The best convergence and median value are obtained from $T = 0.01$. We also notice that we get a wider distribution of values as T decreases. For the value $\kappa = 5$, the median values converge in a nearly identical manner compared to each other. However, the gate freezing provides a better distribution of converged runs when looking at the box plots. The performance of incremental freezing improves as the threshold values decrease. It also outperforms the base **Fraxis** in convergence.

The results in Fig. 18 indicate that the **FQS** benefits significantly from all types of gate freezing. When the freezing iterations are set to $\kappa = 2$, the gate freezing with thresholds $T = 0.01$ and $T = 0.001$ achieves the best median convergence across 20 runs. $T = 0.005$ on the other hand, lacks behind, but demonstrates faster initial convergence than base **FQS**. The distribution of the two previously mentioned thresholds is significantly

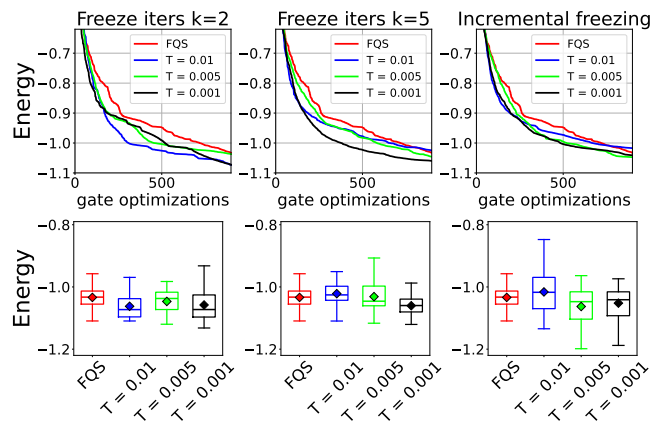


FIG. 18: Results for 6-qubit Fermi-Hubbard model with regular **FQS** (red) and with the matrix norm gate freezing method for 5 layers. Gate freezing threshold was set to $T = 0.01$ (blue), 0.005 (green), 0.001 (black). Freeze iterations $\kappa = 2, 5$ and incremental gate freezing were used.

more concentrated in the ground state compared to that at $T = 0.005$ or the base **FQS**. However, when we set fixed freezing iterations to $\kappa = 5$, the results change. In this scenario, gate freezing with $T = 0.001$ is the best, followed by $T = 0.005$ and base **FQS**. We have similar results for incremental freezing that of $\kappa = 5$, $T = 0.001$, and $T = 0.005$ are the best, followed by the base version of **FQS**, and $T = 0.01$ is the worst. In general, we see that the optimization is enhanced by incorporating gate freezing to **FQS** with matrix norm metric.

C. Scalability

In our final experiment, we investigated the scalability of the proposed method by evaluating the impact of errors as a function of system size, by varying the number of qubits in circuits implementing the Heisenberg model Hamiltonian from Eq. (46). We applied the **Rotosolve** optimizer to quantum circuits characterized with qubit counts ranging from 5 to 15, increments of 2. The number of layers for each circuit was set to $L = n$, where n denotes the number of qubits. The ansatz circuit used in this experiment is the same as the one depicted in Fig. 2. The incremental gate freezing method was employed using gate freezing thresholds of $T = 0.01, 0.005, 0.001$. Each scenario involved a total of 10 runs, with optimization limited to 100 iterations per run. We examined the absolute and relative errors compared to the ground state. The exact ground state of the system was computed using the QuSpin Python package [48].

The results are presented in Fig. 19 as box plots. The base version of **Rotosolve** exhibits the highest absolute and relative error compared to the incremental gate freezing method by varying the qubit count. In comparison

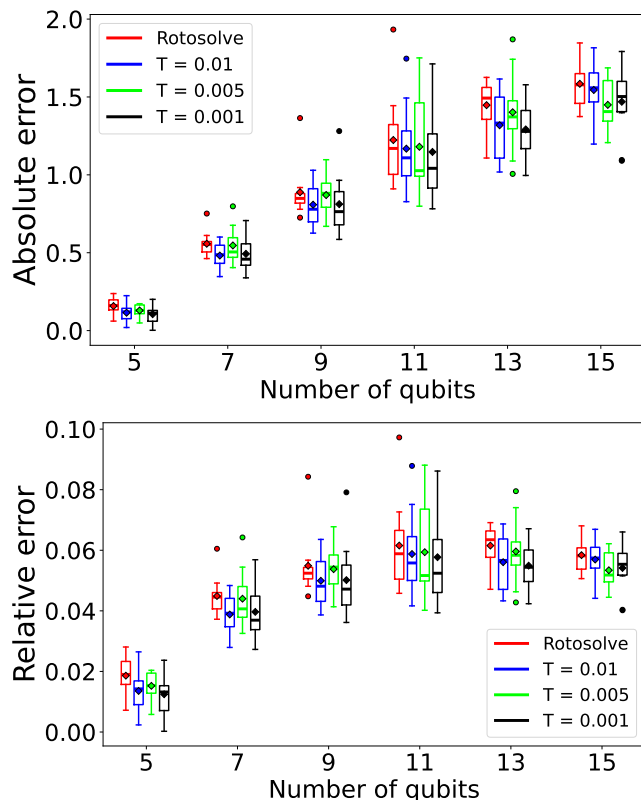


FIG. 19: Absolute (top) and relative (bottom) errors for the Heisenberg model for qubits ranging from 5 to 15, incrementing by 2. The box plots summarize the results for regular *Rotosolve* (red) and the incremental gate freezing method with gate freezing thresholds set to $T = 0.01$ (blue), 0.005 (green), and 0.001 (black). The vertical axis denotes the absolute (relative) error from the true ground state, and the horizontal axis the number of the qubits used in the circuit. The number of layers for each circuit with n qubits was set to $L = n$ according to Fig. 2. The boxes span from the first quartile (Q1) to the third quartile (Q3). The horizontal bar inside the box represents the median, the diamond marker represents the mean, and the whiskers represent values within 1.5 times the interquartile range (IQR). The points outside the range of whiskers are outliers.

to the results in Sec. IV A, we have similar results for 5 qubits. As we increased the number of qubits and layers in the quantum circuits, we observed a growing absolute error relative to the reference ground state. It is important to note that the computational complexity of the optimization process intensifies significantly, given that the size of the system expands exponentially in Hilbert space. Although the absolute error increases with the width of the circuit, the incremental gate freezing method consistently outperforms the base version of *Rotosolve*. However, the relative error only grows until the system size is set to 11 qubits. After that, the relative error stabilizes at to around 0.05.

We also examine the percentage of gates that exceed the set threshold value. In Fig. 20, we show the results in all system sizes ranging from 5 to 15 qubits, incrementing by 2. Here we have plotted the results from an individual run for each number of qubits. Regardless of the system size, we get similar results for all of them. With $T = 0.01$, the percentage of gates exceeding the threshold grows rapidly towards 100 percent. $T = 0.005$ follows tightly behind, but $T = 0.01$ only reaches 30-60 percentage values at the end of the run. In all cases, it has a similar trend in all system sizes, slowly growing over time. We note that the results may vary from run to run, but the overall trend is similar to that shown in Fig. 20.

V. CONCLUSIONS

We have demonstrated through our experiments that, in some cases, gate freezing algorithms enhance the convergence speed and overall performance of existing algorithms *Rotosolve*, *Fraxis*, and *FQS*. Our methods are based on measuring the distance between the previous and new value of each gate after gate optimization, which provides valuable information that has not been extensively used before in the VQAs. Our methods cover both the matrix norm approach and the parameter-wise distance between previous and current gate updates.

The proposed freezing algorithms with fixed threshold T and freeze iterations κ produced results that outperformed their base versions by a significant margin when optimizing the 5-qubit Heisenberg Hamiltonian for *Rotosolve* and *Fraxis*. The *FQS* optimizer, on the other hand, did not receive a significant improvement. By incorporating gate freezing for existing VQAs, one can boost the performance and accuracy of the algorithms.

In addition, we tested a dynamic version of gate freezing, where the number of gate freezes for the specific gate increases by one whenever the gate is frozen. This also produced good results in favor of the freezing algorithms. With *Rotosolve* and *Fraxis*, this was the case, but for the high expressivity algorithm *FQS* it did not give any noticeable advantage when optimizing the complex Fermi-Hubbard Hamiltonian.

We also examined the number of each gates freezing iterations κ_d after the optimization was completed. We found interesting results; the average number of gate freezing iterations κ_d is higher in the later layers compared to the earlier layers. The center qubit in the last layer has the highest average freezing iterations for all optimizers, regardless of the freezing threshold T . This observation is related to the construction of the ansatz circuit; additional results are provided in the Appendix C. With different ansätze, we obtain different gates that are most frozen in the circuit.

Then, we experimented with our methods on the 6-qubit Fermi-Hubbard model on a 1×3 lattice. In some cases, gate freezing led to better results than the base

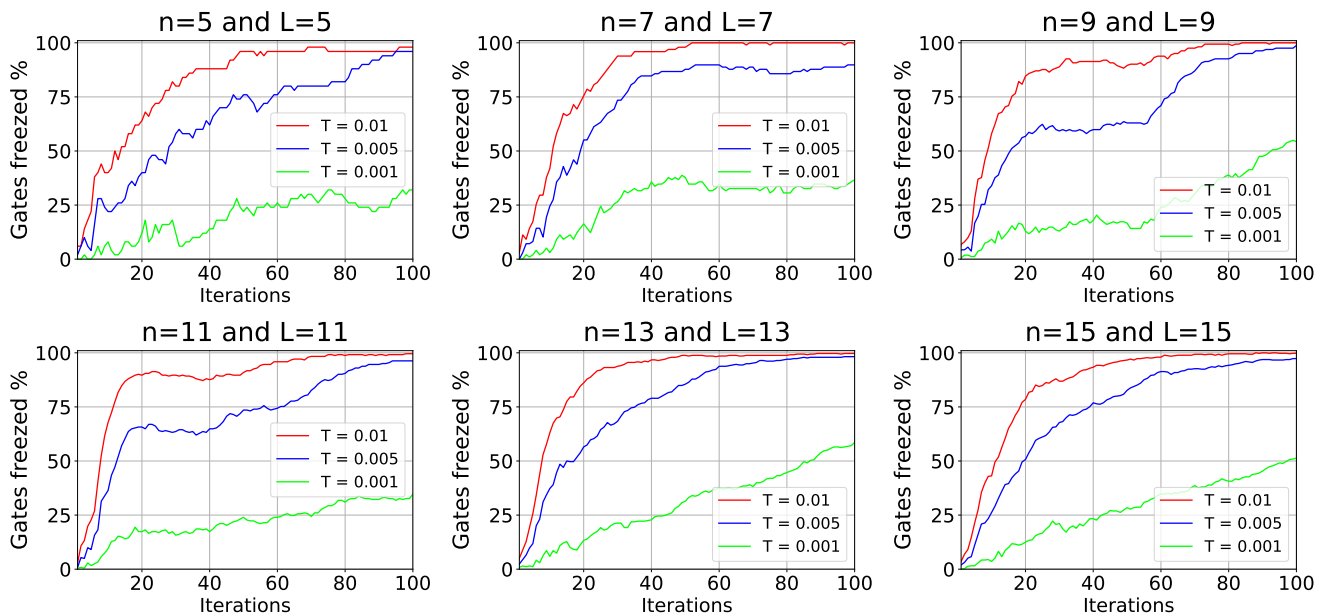


FIG. 20: Results for the Heisenberg model for qubits ranging from 5 to 15, incrementing by 2. The gate freezing thresholds are set to $T = 0.01$ (red), 0.005 (blue), and 0.001 (green). The number of layers for each circuit with n qubits was set to $L = n$ according to Fig. 2.

versions of the algorithms, though not consistently for the parameter distances. The most significant improvement was observed with the FQS optimizer. This aligns with the intuition that more expressive optimizers benefit more from gate freezing when dealing with complex Hamiltonians. In contrast, when optimizing the simpler 5-qubit Heisenberg Hamiltonian, *Rotosolve* benefited the most, which is the opposite of the trend seen with the Fermi-Hubbard model.

Finally, we tested the scalability of the gate freezing method for incremental gate freezing with the *Rotosolve* optimizer using 5 to 15 qubits. The results of the absolute and relative error to the ground state indicate that the gate freezing method is scalable as the complexity of the circuit increases linearly in depth and width simultaneously. That is, as we increase the number of qubits, the layers of the circuit L increase as $\mathcal{O}(n)$. In addition, the percentage of frozen gates in the circuit had the same trend for various thresholds T , regardless of the size of the system.

To conclude this work, we emphasize that our method could be extended to any n -qubit gates using the matrix norm as a distance metric for gate freezing. Our work can also be extended to other types of VQAs by following the idea in Sec. III A if parameter-based gate freezing is desired.

The results for the number of gate freezing iterations in Sec. IV A 3 provide an interesting insight into how the parameters change on average during the optimization process. This indicates that there may be better ways to create the gate optimization sequence, especially for the *Fraxis* and FQS optimizers. We intend to explore

this behavior further and how to utilize it in the PQC optimization.

VI. DATA AVAILABILITY

The source code and data to generate the figures in the paper are available at Ref. [49].

ACKNOWLEDGMENTS

We acknowledge funding by Business Finland for the project 8726/31/2022 CICAQU. J.P. received funding from InstituteQ’s doctoral school.

Appendix A: Ansatz Circuits

Here, we provide ansatz circuits used in additional experiments in the Appendices C and D. Ansatz type B is illustrated in Fig. 21, type C in Fig. 22, and type D in Fig. 23.

Appendix B: Additional experiments – Threshold counts without gate freezing

In this section, we provide additional experiments relating to Sec. IV A 3. We use *Fraxis* and FQS optimizers with matrix norm-based gate freezing, but only collect data if the difference between gate parameters exceeds

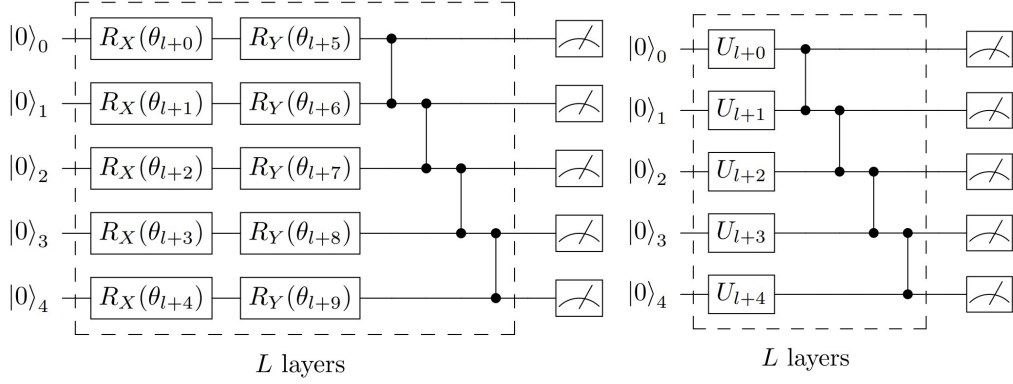


FIG. 21: Ansatz circuits B1 (left) and B2 (right) with a cascade entangling layer.

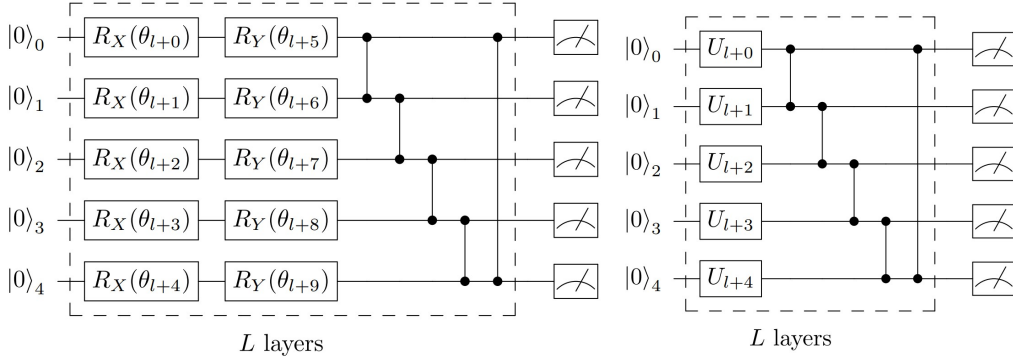


FIG. 22: Ansatz circuits C1 (left) and C2 (right) with a cyclic entangling layer.

the threshold value. This basically means that we run base versions of the VQAs since no gate freezing is taking place, and thus no gate optimizations are saved.

We have similar results to those for the gate freezing case with parameter-based gate freezing. For **Fraxis**, in Fig. 24 we see that when we freeze gates based on matrix norms, the middle qubits gate in the last layer receives the most gate freezes for all thresholds T . If we compare $T = 0.001$ with the parameter distance from Sec. IV A 3, the matrix norm exhibits a more symmetrical pattern. Otherwise, gate freezing does not seem to be affected by whether we choose the matrix norm or parameter distance as the gate freezing metric. For the **FQS** optimizer in Fig. 25 and Sec. IV A 3, there is no difference for the matrix norm freezing versus the parameter distance freezing.

Appendix C: Additional experiments – Threshold counts without gate freezing with other circuit Ansätze

In this section, we provide additional results for the gate freezing iterations, similar to Sec. IV A 3 but with different ansatz circuits (types B, C, and D). The circuits are provided in the Appendix A. For all optimizers, we use the parameter-based gate freezing method.

The additional results for **Rotosolve** optimizer are shown in Fig. 26. Each row corresponds to the results for different ansatz circuits B1 (cascade), C1 (cyclic entangling), and D1 (one-qubit connector) from Appendix A, respectively. For ansatz circuit B1, we have similar results as in Sec. IV A 3. If the threshold is set to $T = 0.001$, the B1 and C1 share a similar structure that both have the most gate freezes in the last layer, but for the C1 ansatz, they are spread out and not concentrated for the single qubit as in B1. Ansatz D1 seems to have no clear structure when compared to B1 and C1. Furthermore, no clear pattern emerges, except that some gates on the first qubit have the most gate freezes. Also, with $T = 0.01$ and $T = 0.005$ for the D1 Ansatz, the gate freezes are more focused on the first layer of the circuit, respectively.

The results for **Fraxis** are shown in Fig. 27. For $T = 0.01$, all ansätze have about the same behavior, where the gates in the first layer are less often frozen compared to the rest. When we set $T = 0.005$, the results are similar, except for the ansatz D2. The gates in the second layer are frozen more frequently than those in the first and last layers. The gate freezes are more spread out compared to other ansatz circuits, as in **Rotosolve**'s case. Finally, when we set $T = 0.001$, the gates in the first and second layers have similar low average values for ansätze B2 and C2. The most frozen gate for D2 is the first gate in the optimization sequence, the top left gate. The least frozen

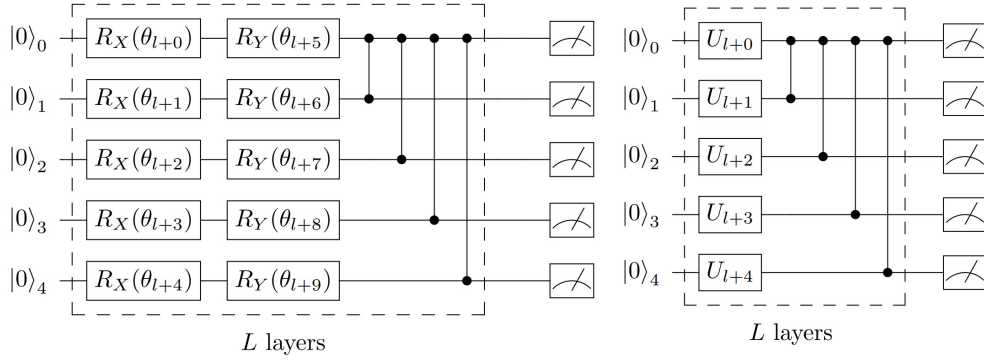


FIG. 23: Ansatz circuits D1 (left) and D2 (right) with a one-qubit connector entangling layer.

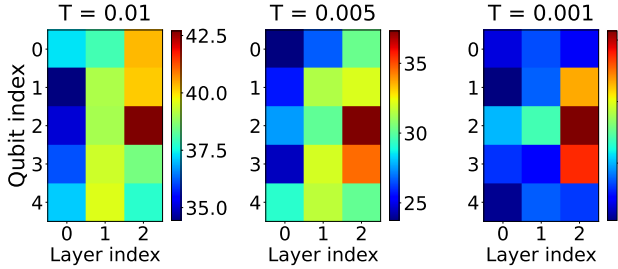


FIG. 24: Results for 5-qubit Heisenberg model without gate freezing method for 3 layers with **Fraxis** algorithm. The gate freezing threshold T was set to have values $T = 0.01$ (left), 0.005 (mid) and 0.001 (right). Each block in the grid represents the mean of the gate freeze iterations of 50 runs. Red cells of the grid indicate a higher average and blue cells a lower average value.

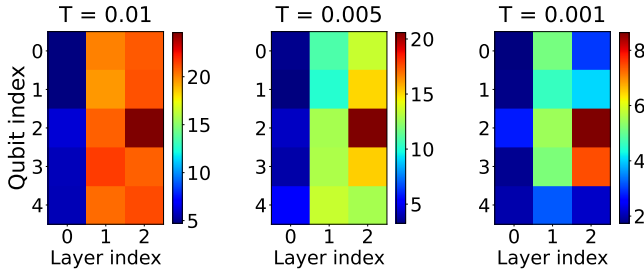


FIG. 25: Results for 5-qubit Heisenberg model without gate freezing method for 3 layers with **FQS** algorithm. The gate freezing threshold T was set to have values $T = 0.01$ (left), 0.005 (mid), and 0.001 (right). Each block in the grid represents the mean of the gate freeze iterations of 50 runs. Red cells of the grid indicate a higher average and blue cells a lower average value.

gates are located in the last layer, primarily affecting qubits with lower indices.

Finally, we present our results for the **FQS** optimizer, which are shown in Fig. 28. With the gate freezing threshold value $T = 0.01$, the first layer of all ansätze

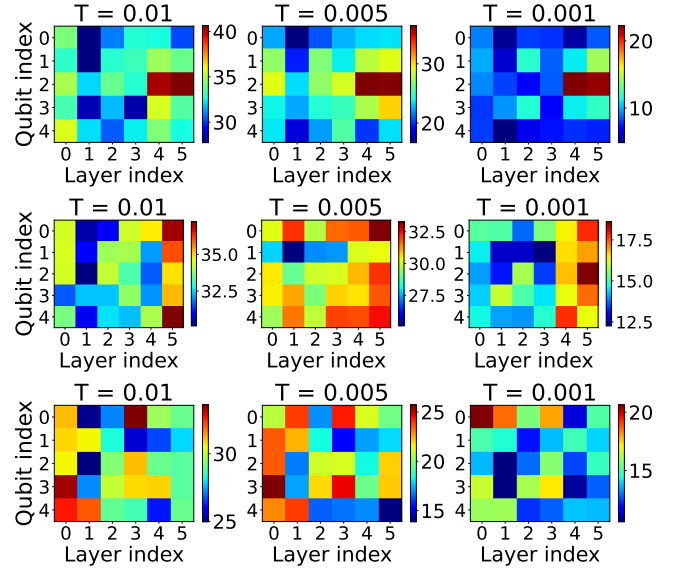


FIG. 26: Results for 5-qubit Heisenberg model without gate freezing method for 3 layers with **Rotosolve** algorithm. The gate freezing threshold T was set to have values $T = 0.01$, 0.005 , and 0.001 , which are shown in the left, middle, and right columns, respectively. Each row corresponds to ansatz circuits B1, C1, and D1 from Appendix A, respectively, and each block in the grid represents the mean of the gate freeze iterations of 50 runs. Red cells of the grid indicate a higher average and blue cells a lower average value.

receives the least amount of gate freezes, such as **Fraxis**. When we set $T = 0.005$, the gate freezes for the ansatz B2 concentrates more and more on the center of the last layer. On the other hand, the most frozen gates are distributed evenly in the last layer for the C2 ansatz and oddly enough in the second layer for the D2 ansatz. Finally, when the threshold is set to $T = 0.001$, the most frozen gate in D2 is exactly in the middle of the circuit. The results for Ansatz B2 appear nearly identical to those shown in the Appendix B. Ansatz C2 has frozen gates at the top and bottom, and more gates are frozen overall

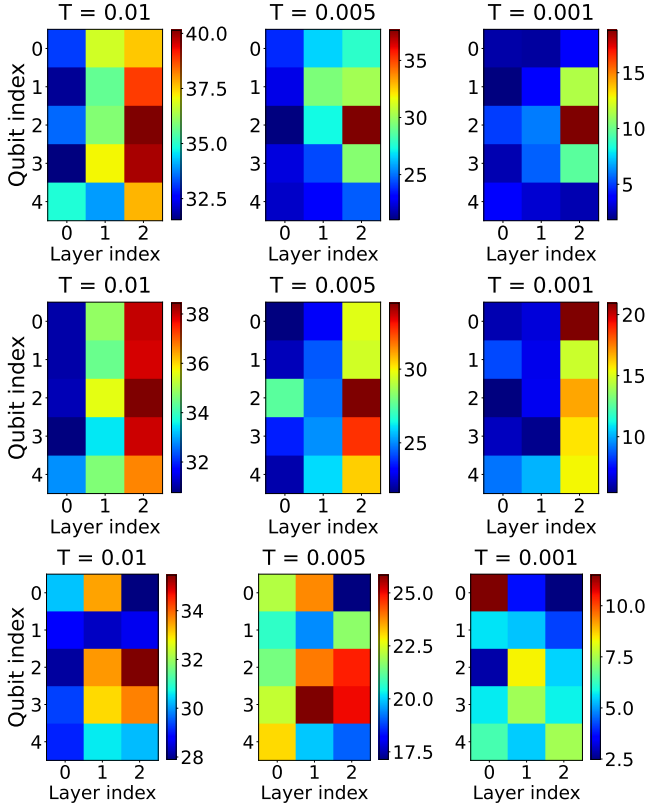


FIG. 27: Results for 5-qubit Heisenberg model without gate freezing method for 3 layers with Fraxis algorithm. The gate freezing threshold T was set to have values $T = 0.01, 0.005,$ and 0.001 are shown in the left, middle, and right columns, respectively. Each row corresponds to ansatz circuits B2, C2, and D2 from Appendix A, respectively, and each block in the grid represents the mean of the gate freeze iterations of 50 runs. Red cells of the grid indicate a higher average and blue cells a lower average value.

for the last two layers compared to the B2 or D2 circuits.

Appendix D: Mutual Information Between the Qubits in Different Ansätze

This section presents an analysis of mutual information heat maps between qubits for different ansatz circuit types A–D, each consisting of 5 qubits and 3 layers. This investigation aims to provide a more accurate metric for evaluating correlations observed in the gate freezing heat maps. Ansatz circuit type A is shown in Fig. 2, while types B–D are provided in Appendix A.

The mutual information between two quantum subsystems, P and Q , forming a joint state described by the bipartite density matrix ρ_{PQ} , is defined as the real-valued

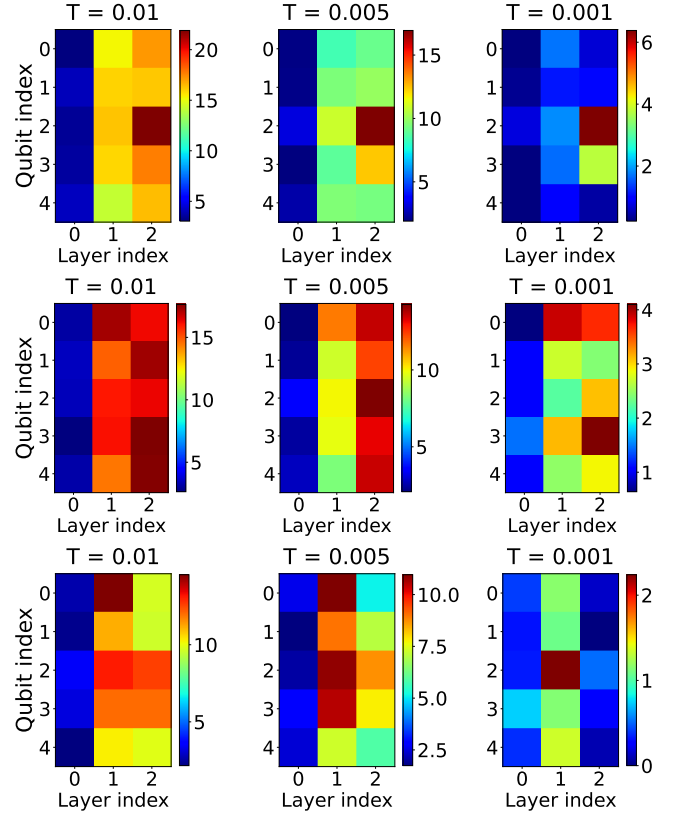


FIG. 28: Results for 5-qubit Heisenberg model without gate freezing method for 3 layers with FQS algorithm. The gate freezing threshold T was set to have values $T = 0.01, 0.005,$ and 0.001 are shown in the left, middle, and right columns, respectively. Each row corresponds to ansatz circuits B2, C2, and D2 from Appendix A, respectively, and each block in the grid represents the mean of the gate freeze iterations of 50 runs. Red cells of the grid indicate a higher average and blue a lower average value.

quantity $I(P : Q)$ [41]. It is computed as:

$$I(P : Q) = S(\rho_P) + S(\rho_Q) - S(\rho_{PQ}), \quad (D1)$$

where $S(\rho_P)$ denotes the von Neumann entropy, defined as $S(\rho_P) = -\text{Tr}[\rho_P \log \rho_P]$ and ρ_P , and ρ_Q are the reduced density matrices of ρ_{PQ} [41].

Mutual information quantifies the total correlations, both classical and quantum, between subsystems P and Q . It serves as a key tool for understanding the structural and behavioral properties of quantum circuits [50, 51]. Unlike measures that capture only quantum correlations, such as entanglement entropy, mutual information includes all forms of correlation and therefore serves as an upper bound to more specific quantities like entanglement of formation or quantum discord [52–54]. In the context of PQC, mutual information offers insight into a circuit’s expressibility and entangling capability [55, 56]. Evaluating mutual information between all

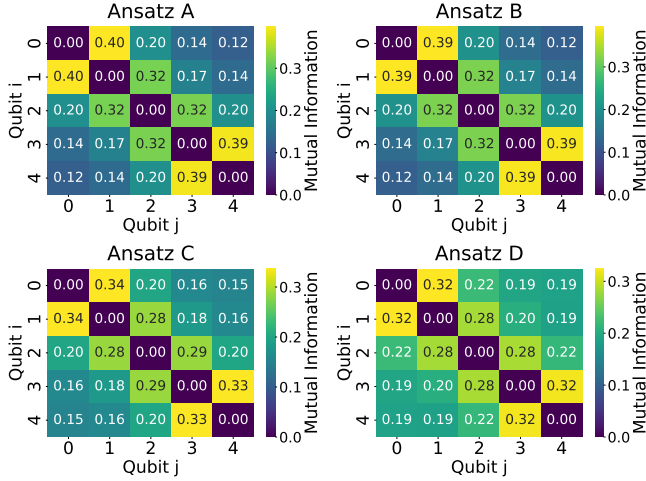


FIG. 29: Heatmap of the mutual information between qubit pairs for different ansatz circuit types A–D with **Rotosolve** optimizer. Yellow indicates higher mutual information between the qubits, whereas dark blue lower value.

pairs of qubits across different ansatz types reveals how quantum correlations are distributed and how information propagates through the circuit. High mutual information between distant qubits may indicate long-range entanglement or strong connectivity, potentially impacting the performance of VQAs [57]. Next, we present our results on mutual information between qubits of the PQC for ansatz types A–D.

We conducted our analysis by drawing 10^4 samples for each ansatz type using the **Rotosolve**, **Fraxis**, and **FQS** optimizers, all configured with 3 layers. In each sample, circuit parameters were sampled from the uniform distribution associated with each optimizer, as described in Sec IV. For each sampled circuit, we obtained the output quantum state, computed the corresponding density matrix, and evaluated the mutual information matrix across all qubit pairs. The final heat maps represent the average mutual information values between qubit pairs across all samples. The results for **Rotosolve**, **Fraxis** and **FQS** are shown in Fig. 29, Fig. 30 and Fig. 31, respectively.

Across all optimizers, we observed that ansatz types produce almost exact mutual information heatmaps, despite minor variations in entanglement structure. In particular, nearest-neighbor qubit pairs ($i, i \pm 1$) exhibit the highest mutual information values. For circuit types C and D, mutual information between non-neighboring (i.e., off-diagonal) qubit pairs increases noticeably.

Finally, we compare these mutual information heat maps with the gate freezing heat maps shown in Appendix C and Sec. III C. Ansatz circuits A and B exhibit similar patterns in both mutual information and gate freezing heat maps. In contrast, circuit types C and D display distinct differences in both metrics. These findings suggest a correlation: when mutual information

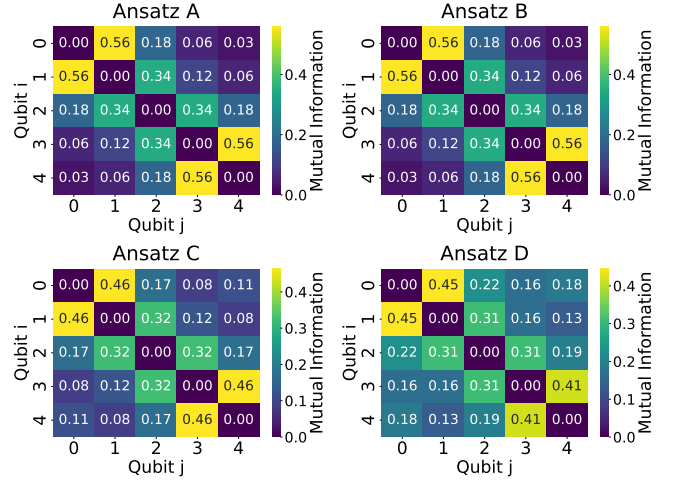


FIG. 30: Heatmap of the mutual information between qubit pairs for different ansatz circuit types A–D with **Fraxis** optimizer. Yellow indicates higher mutual information between the qubits, whereas dark blue indicates a lower value.

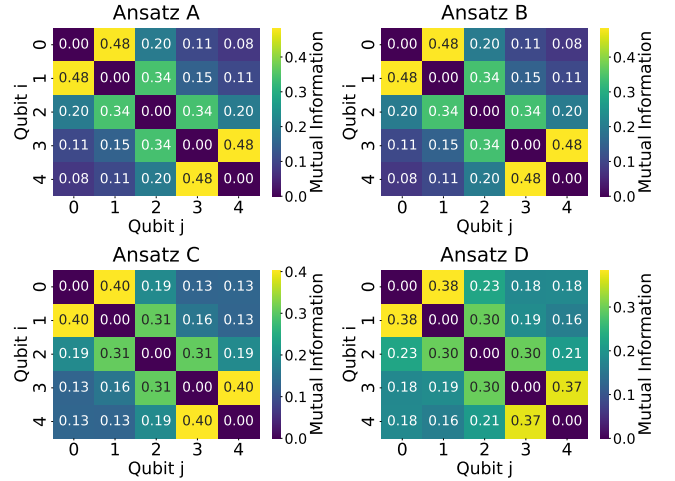


FIG. 31: Heatmap of the mutual information between qubit pairs for different ansatz circuit types A–D with **FQS** optimizer. Yellow indicates higher mutual information between the qubits, whereas dark blue indicates a lower value.

heat maps are similar, the corresponding gate freezing heat maps also tend to resemble one another, regardless of structural differences in the ansatz circuits.

Appendix E: Scaling Matrix Norms

In this section, we explore the implementation of gate freezing for various gate sizes. Before evaluating whether the optimized gate surpasses the freezing threshold, we normalize the computed norm values to a common range. Matrix norms vary in their range of values depending

on the size of the unitary matrices. To allow consistent comparison across different matrix sizes, we normalize all calculated norm values to lie within the range $[0, 1]$.

We focus on the distance metric derived from the Frobenius norm in Sec. III B. Let U and V be unitary matrices of size $2^n \times 2^n$. The Frobenius norm between matrices U and V is defined:

$$\|U - V\|_F = \sqrt{\text{Tr}[(U - V)^\dagger(U - V)]}, \quad (\text{E1})$$

Using the fact that $\text{Tr}(U^\dagger U) = \text{Tr}(V^\dagger V) = \text{Tr}(I) = 2^n$ for n -qubit unitaries, we then obtain

$$\|U - V\|_F = \sqrt{2^{n+1} - 2 \cdot \text{Re}(\text{Tr}(U^\dagger V))}. \quad (\text{E2})$$

By a similar argument as in Sec. III B, we rotate the Frobenius inner product $\text{Tr}(U^\dagger V)$ onto the positive real axis with the complex phase $e^{i\delta}$. That is, we select δ such that $\text{Tr}(U^\dagger e^{i\delta} V) = e^{i\delta} \text{Tr}(U^\dagger V) = |\text{Tr}(U^\dagger V)|$. Then the expression for the n -qubit unitaries becomes

$$\mathcal{D}(U, V) = \sqrt{2^{n+1} - 2 \cdot |\text{Tr}(U^\dagger V)|}. \quad (\text{E3})$$

Finally, as in Sec. III B, we normalize the distance to be in the range $[0, 1]$. The expression inside the square root achieves its maximal value when $|\text{Tr}(U^\dagger V)| = 0$ and hence $\mathcal{D}(U, V)$ can have a maximal value of $\sqrt{2^{n+1}}$. To obtain the normalized distance for the n -qubit unitaries, we divide the computed distance by its maximal value $\sqrt{2^{n+1}}$.

-
- [1] M. Cerezo, A. Arrasmith, R. Babbush, S. C. Benjamin, S. Endo, K. Fujii, J. R. McClean, K. Mitarai, X. Yuan, L. Cincio, *et al.*, Variational quantum algorithms, *Nature Reviews Physics* **3**, 625 (2021).
- [2] A. Peruzzo, J. McClean, P. Shadbolt, M.-H. Yung, X.-Q. Zhou, P. J. Love, A. Aspuru-Guzik, and J. L. O’Brien, A variational eigenvalue solver on a photonic quantum processor, *Nature communications* **5**, 4213 (2014).
- [3] B. Bauer, S. Bravyi, M. Motta, and G. K.-L. Chan, Quantum algorithms for quantum chemistry and quantum materials science, *Chemical reviews* **120**, 12685 (2020).
- [4] H. Singh, S. Majumder, and S. Mishra, Benchmarking of different optimizers in the variational quantum algorithms for applications in quantum chemistry, *The Journal of Chemical Physics* **159** (2023).
- [5] A. Delgado, J. M. Arrazola, S. Jahangiri, Z. Niu, J. Izaac, C. Roberts, and N. Killoran, Variational quantum algorithm for molecular geometry optimization, *Physical Review A* **104**, 052402 (2021).
- [6] M. Motta and J. E. Rice, Emerging quantum computing algorithms for quantum chemistry, *Wiley Interdisciplinary Reviews: Computational Molecular Science* **12**, e1580 (2022).
- [7] Y. Cao, J. Romero, J. P. Olson, M. Degroote, P. D. Johnson, M. Kieferová, I. D. Kivlichan, T. Menke, B. Peropadre, N. P. Sawaya, *et al.*, Quantum chemistry in the age of quantum computing, *Chemical reviews* **119**, 10856 (2019).
- [8] M. Svensson, M. Andersson, M. Grönkvist, P. Vikstål, D. Dubhashi, G. Ferrini, and G. Johansson, Hybrid quantum-classical heuristic to solve large-scale integer linear programs, *Phys. Rev. Appl.* **20**, 034062 (2023).
- [9] G. E. Crooks, Performance of the quantum approximate optimization algorithm on the maximum cut problem, *arXiv preprint arXiv:1811.08419* (2018).
- [10] P. Vikstål, M. Grönkvist, M. Svensson, M. Andersson, G. Johansson, and G. Ferrini, Applying the quantum approximate optimization algorithm to the tail-assignment problem, *Physical Review Applied* **14**, 034009 (2020).
- [11] J. Liu, K. H. Lim, K. L. Wood, W. Huang, C. Guo, and H.-L. Huang, Hybrid quantum-classical convolutional neural networks, *Science China Physics, Mechanics & Astronomy* **64**, 290311 (2021).
- [12] D. Arthur and P. Date, Hybrid quantum-classical neural networks, in *2022 IEEE International Conference on Quantum Computing and Engineering (QCE)* (IEEE, 2022) pp. 49–55.
- [13] S. Jerbi, L. J. Fiderer, H. Poulsen Nautrup, J. M. Kübler, H. J. Briegel, and V. Dunjko, Quantum machine learning beyond kernel methods, *Nature Communications* **14**, 517 (2023).
- [14] J. Shi, W. Wang, X. Lou, S. Zhang, and X. Li, Parameterized hamiltonian learning with quantum circuit, *IEEE Transactions on Pattern Analysis and Machine Intelligence* **45**, 6086 (2022).
- [15] J. R. McClean, J. Romero, R. Babbush, and A. Aspuru-Guzik, The theory of variational hybrid quantum-classical algorithms, *New Journal of Physics* **18**, 023023 (2016).
- [16] M. Benedetti, E. Lloyd, S. Sack, and M. Fiorentini, Parameterized quantum circuits as machine learning models, *Quantum science and technology* **4**, 043001 (2019).
- [17] A. Kandala, A. Mezzacapo, K. Temme, M. Takita, M. Brink, J. M. Chow, and J. M. Gambetta, Hardware-efficient variational quantum eigensolver for small molecules and quantum magnets, *nature* **549**, 242 (2017).
- [18] P. J. O’Malley, R. Babbush, I. D. Kivlichan, J. Romero, J. R. McClean, R. Barends, J. Kelly, P. Roushan, A. Tranter, N. Ding, *et al.*, Scalable quantum simulation of molecular energies, *Physical Review X* **6**, 031007 (2016).
- [19] L. Bittel and M. Müller, Training of quantum circuits: A review of recent developments, *arXiv preprint arXiv:2102.01604* (2021).
- [20] S. Hadfield, Z. Wang, B. O’gorman, E. G. Rieffel, D. Venturelli, and R. Biswas, From the quantum approximate optimization algorithm to a quantum alternating operator ansatz, *Algorithms* **12**, 34 (2019).
- [21] Z. Wang, S. Hadfield, Z. Jiang, and E. G. Rieffel, Quantum approximate optimization algorithm for maxcut: A fermionic view, *Physical Review A* **97**, 022304 (2018).
- [22] K. Bharti, A. Cervera-Lierta, T. H. Kyaw, T. Haug, S. Alperin-Lea, A. Anand, M. Degroote, H. Heimonen,

- J. S. Kottmann, T. Menke, W.-K. Mok, S. Sim, L.-C. Kwek, and A. Aspuru-Guzik, Noisy intermediate-scale quantum algorithms, *Rev. Mod. Phys.* **94**, 015004 (2022).
- [23] B. Bertini, F. Heidrich-Meisner, C. Karrasch, T. Prosen, R. Steinigeweg, and M. Žnidarič, Finite-temperature transport in one-dimensional quantum lattice models, *Rev. Mod. Phys.* **93**, 025003 (2021).
- [24] K. Mitarai, M. Negoro, M. Kitagawa, and K. Fujii, Quantum circuit learning, *Physical Review A* **98**, 032309 (2018).
- [25] J. Preskill, Quantum computing in the nisq era and beyond, *Quantum* **2**, 79 (2018).
- [26] M. Schuld, A. Bocharov, K. M. Svore, and N. Wiebe, Circuit-centric quantum classifiers, *Physical Review A* **101**, 032308 (2020).
- [27] J. R. McClean, S. Boixo, V. N. Smelyanskiy, R. Babush, and H. Neven, Barren plateaus in quantum neural network training landscapes, *Nature communications* **9**, 4812 (2018).
- [28] M. Cerezo, A. Sone, T. Volkoff, L. Cincio, and P. J. Coles, Cost function dependent barren plateaus in shallow parametrized quantum circuits, *Nature communications* **12**, 1791 (2021).
- [29] K. Zhang, L. Liu, M.-H. Hsieh, and D. Tao, Escaping from the barren plateau via gaussian initializations in deep variational quantum circuits, *Advances in Neural Information Processing Systems* **35**, 18612 (2022).
- [30] X. Shi and Y. Shang, Avoiding barren plateaus via gaussian mixture model, *arXiv preprint arXiv:2402.13501* (2024).
- [31] Y. Wang, B. Qi, C. Ferrie, and D. Dong, Trainability enhancement of parameterized quantum circuits via reduced-domain parameter initialization, *Physical Review Applied* **22**, 054005 (2024).
- [32] X. Lee, Y. Saito, D. Cai, and N. Asai, Parameters fixing strategy for quantum approximate optimization algorithm, *2021 IEEE International Conference on Quantum Computing and Engineering (QCE)*, 10 (2021).
- [33] E. Farhi, J. Goldstone, and S. Gutmann, A quantum approximate optimization algorithm, *arXiv preprint arXiv:1411.4028* (2018).
- [34] A. Skolik, J. R. McClean, M. Mohseni, P. Van Der Smagt, and M. Leib, Layerwise learning for quantum neural networks, *Quantum Machine Intelligence* **3**, 1 (2021).
- [35] S. Sim, J. Romero, J. F. Gonthier, and A. A. Kunitsa, Adaptive pruning-based optimization of parameterized quantum circuits, *Quantum Science and Technology* **6**, 025019 (2021).
- [36] M. Ostaszewski, E. Grant, and M. Benedetti, Structure optimization for parameterized quantum circuits, *Quantum* **5**, 391 (2021).
- [37] H. C. Watanabe, R. Raymond, Y. ya Ohnishi, E. Kaminishi, and M. Sugawara, *Optimizing parameterized quantum circuits with free-axis selection* (2023), *arXiv:2104.14875* [quant-ph].
- [38] K. Wada, R. Raymond, Y. Sato, and H. C. Watanabe, Sequential optimal selections of single-qubit gates in parameterized quantum circuits, *Quantum Science and Technology* **9**, 035030 (2024).
- [39] J. V. Pankkonen, L. Ylinen, M. Raasakka, and I. Tittonen, *Improving variational quantum circuit optimization via hybrid algorithms and random axis initialization* (2025), *arXiv:2503.20728* [quant-ph].
- [40] N. Moll, P. Barkoutsos, L. S. Bishop, J. M. Chow, A. Cross, D. J. Egger, S. Filipp, A. Fuhrer, J. M. Gambetta, M. Ganzhorn, *et al.*, Quantum optimization using variational algorithms on near-term quantum devices, *Quantum Science and Technology* **3**, 030503 (2018).
- [41] M. A. Nielsen and I. L. Chuang, *Quantum computation and quantum information* (Cambridge university press, 2010).
- [42] V. Bergholm, J. Izaac, M. Schuld, C. Gogolin, S. Ahmed, V. Ajith, M. S. Alam, G. Alonso-Linaje, B. Akash-Narayanan, A. Asadi, J. M. Arrazola, U. Azad, S. Banning, C. Blank, T. R. Bromley, B. A. Cordier, J. Ceroni, A. Delgado, O. D. Matteo, A. Dusko, T. Garg, D. Guala, A. Hayes, R. Hill, A. Ijaz, T. Isaacson, D. Ittah, S. Jahangiri, P. Jain, E. Jiang, A. Khandelwal, K. Kottmann, R. A. Lang, C. Lee, T. Loke, A. Lowe, K. McKiernan, J. J. Meyer, J. A. Montañez-Barrera, R. Moyard, Z. Niu, L. J. O’Riordan, S. Oud, A. Panigrahi, C.-Y. Park, D. Polatajko, N. Quesada, C. Roberts, N. Sá, I. Schoch, B. Shi, S. Shu, S. Sim, A. Singh, I. Strandberg, J. Soni, A. Száva, S. Thabet, R. A. Vargas-Hernández, T. Vincent, N. Vitucci, M. Weber, D. Wierichs, R. Wiersema, M. Willmann, V. Wong, S. Zhang, and N. Killoran, *Penylane: Automatic differentiation of hybrid quantum-classical computations* (2022), *arXiv:1811.04968* [quant-ph].
- [43] W. Heisenberg, Über die quantentheoretische umdeutung kinematischer und mechanischer beziehungen, *Zeitschrift für Physik* **43**, 172 (1928).
- [44] J. Hubbard, Electron correlations in narrow energy bands, *Proc. Roy. Soc. (London), Ser. A* **Vol: 276**, 10.1098/rspa.1963.0204 (1963).
- [45] T. Esslinger, Fermi-hubbard physics with atoms in an optical lattice, *Annual Review of Condensed Matter Physics* **1**, 129–152 (2010).
- [46] A. Altland and B. Simons, *Condensed Matter Field Theory*, Cambridge books online (Cambridge University Press, 2010).
- [47] E. Wigner and P. Jordan, Über das paulische äquivalenzverbot, *Z. Phys* **47**, 46 (1928).
- [48] P. Weinberg and M. Bukov, Quspin: a python package for dynamics and exact diagonalisation of quantum many body systems part i: spin chains, *SciPost Physics* **2**, 003 (2017).
- [49] https://github.com/joonpank/PQC_Optimization_Gate_Freezing, [Accessed 18-06-2025].
- [50] M. Tisoc and J. V. Beltrán, Mutual information: A way to quantify correlations, *Revista Brasileira de Ensino de Física* **44**, e20220055 (2022).
- [51] K. Modi, A. Brodutch, H. Cable, T. Paterek, and V. Vedral, The classical-quantum boundary for correlations: Discord and related measures, *Rev. Mod. Phys.* **84**, 1655 (2012).
- [52] L. Henderson and V. Vedral, Classical, quantum and total correlations, *Journal of Physics A: Mathematical and General* **34**, 6899–6905 (2001).
- [53] M. Horodecki, J. Oppenheim, and A. Winter, Partial quantum information, *Nature* **436**, 673 (2005).
- [54] G. De Chiara and A. Sanpera, Genuine quantum correlations in quantum many-body systems: a review of recent progress, *Reports on Progress in Physics* **81**, 074002 (2018).
- [55] S. Sim, P. D. Johnson, and A. Aspuru-Guzik, Expressibility and entangling capability of parameterized quan-

- tum circuits for hybrid quantum-classical algorithms, *Advanced Quantum Technologies* **2**, 1900070 (2019).
- [56] A. Anand, L. B. Kristensen, F. Frohnert, S. Sim, and A. Aspuru-Guzik, Information flow in parameterized quantum circuits, *Quantum Science and Technology* **9**, 035025 (2024).
- [57] Z. Holmes, K. Sharma, M. Cerezo, and P. J. Coles, Connecting ansatz expressibility to gradient magnitudes and barren plateaus, *PRX quantum* **3**, 010313 (2022).